

THE ARECIBO LEGACY FAST ALFA SURVEY: THE GALAXY POPULATION DETECTED BY ALFALFA

SHAN HUANG, MARTHA P. HAYNES, RICCARDO GIOVANELLI

Center for Radiophysics and Space Research, Space Sciences Building, Cornell University, Ithaca, NY 14853.

JARLE BRINCHMANN

Sterrewacht Leiden, Leiden University, NL-2300 RA Leiden, The Netherlands

Draft version Wednesday 27th November, 2024

ABSTRACT

Making use of HI 21 cm line measurements from the ALFALFA survey ($\alpha.40$) and photometry from the Sloan Digital Sky Survey (SDSS) and GALEX, we investigate the global scaling relations and fundamental planes linking stars and gas for a sample of 9417 common galaxies: the $\alpha.40$ -SDSS-GALEX sample. In addition to their HI properties derived from the ALFALFA dataset, stellar masses (M_*) and star formation rates (SFRs) are derived from fitting the UV-optical spectral energy distributions. 96% of the $\alpha.40$ -SDSS-GALEX galaxies belong to the blue cloud, with the average gas fraction $f_{HI} \equiv M_{HI}/M_* \sim 1.5$. A transition in SF properties is found whereby below $M_* \sim 10^{9.5} M_\odot$, the slope of the star forming sequence changes, the dispersion in the specific star formation rate (SSFR) distribution increases and the star formation efficiency (SFE) mildly increases with M_* . The evolutionary track in the SSFR- M_* diagram, as well as that in the color magnitude diagram are linked to the HI content; below this transition mass, the star formation is regulated strongly by the HI. Comparison of HI- and optically-selected samples over the same restricted volume shows that the HI-selected population is less evolved and has overall higher SFR and SSFR at a given stellar mass, but lower SFE and extinction, suggesting either that a bottleneck exists in the HI to H₂ conversion, or that the process of SF in the very HI-dominated galaxies obeys an unusual, low efficiency star formation law. A trend is found that, for a given stellar mass, high gas fraction galaxies reside preferentially in dark matter halos with high spin parameters. Because it represents a full census of HI-bearing galaxies at $z \sim 0$, the scaling relations and fundamental planes derived for the ALFALFA population can be used to assess the HI detection rate by future blind HI surveys and intensity mapping experiments at higher redshift.

Subject headings: galaxies: evolution – galaxies: fundamental parameters – galaxies: ISM – galaxies: star formation – radio lines: galaxies – surveys

1. INTRODUCTION

In the last decade, the galaxy catalogs contributed by legacy programs like the Sloan Digital Sky Survey (SDSS) and the Galaxy Evolution Explorer (GALEX) satellite extragalactic surveys have enabled us to quantify properties associated with the stellar populations of galaxies in the local universe. Through their statistically-based insight into the stellar component and the interrelationship of the physical parameters, these surveys have provided quantitative clues of importance to our understanding of the formation and evolution of galaxies (e.g. Brinchmann et al. 2004; Salim et al. 2007). The bimodal distribution evident in the color-magnitude diagram (Baldry et al. 2004; Schiminovich et al. 2007) suggests a likely evolution scenario whereby galaxies in the blue cloud form stars vigorously and grow through mergers and later, after depleting their gas reservoirs, then migrate to the red sequence. This picture is also supported by tracers of the star formation history (SFH): e.g., the specific star formation rate (SSFR), the star formation rate (SFR) per unit stellar mass, is seen to vary with the total stellar mass (Brinchmann et al. 2004). The star-forming sequence (high SSFR) is associated with actively star forming blue cloud galaxies. Indeed, the stellar mass appears to be the crucial quantity governing the star formation (SF) along this sequence. In the absence of mergers or other events that trigger a starburst, blue galaxies

on the sequence evolve towards higher stellar mass and lower SSFR, and eventually become red and dead.

In statistical terms, all surveys are biased by the properties that define them. For example, optical surveys are biased in terms of optical flux and possibly surface brightness. The SDSS legacy galaxy redshift sample has an apparent r -band Petrosian magnitude limit of 17.77, as well as a surface brightness limit of 23.0 mag arcsec⁻² at the half light radius in r (Strauss et al. 2002). In contrast, blind HI surveys are unbiased by optical characteristics but have their own limitations in terms of HI line emission sensitivity, usually as a function of HI line width (Martin et al. 2010; Haynes et al. 2011). Because M_{HI}/L_{opt} increases with decreasing L_{opt} , HI-selected samples are more inclusive of star-forming galaxies than optical samples of similar depth. Indeed, since almost all star-forming galaxies contain neutral gas, an HI-selected sample can approach a full census of star-forming galaxies. For example, West et al. (2010) demonstrated the HI-selection identifies galaxies with lower surface brightness, smaller absolute magnitudes, bluer colors and smaller stellar masses than those used in typical SDSS studies. However, the limitation with an HI-selected sample is that it will miss the early type galaxies, which contain very little neutral gas (Garcia-Appadoo et al. 2009). Furthermore, analysis of the spatial correlation function $\xi(r)$ shows that the HI-selected galaxies represent the least clustered population on small scales (Martin et al. 2012), a fact important for interpreting the results of future HI intensity mapping experiments.

Exploiting the mapping capability of the Arecibo L-band feed array (ALFA) and the sensitivity of the Arecibo 305 m antenna, the Arecibo Legacy Fast ALFA (ALFALFA) survey (Giovanelli et al. 2005a,b) is an ongoing blind HI survey, aimed at mapping ~ 7000 square degrees of high galactic latitude sky between 0° and $+36^\circ$ in declination. When complete, the survey will detect more than 30,000 galaxies out to redshift of 0.06 with a median recession velocity, cz , of $\sim 8200 \text{ km s}^{-1}$ (Haynes et al. 2011). Compared to the HI Parkes All Sky Survey (HIPASS: Barnes et al. 2001; Meyer et al. 2004; Wong et al. 2006), ALFALFA is 8 times more sensitive, its spectral coverage extends over 1.6 times the bandwidth of HIPASS, and the angular resolution of ALFA is 4 times better than that of the Parkes multifield receiver. The combination of sensitivity and spectral bandwidth enables ALFALFA to detect thousands of massive HI disks with $M_{HI} > 10^{10} M_\odot$. In addition, the Arecibo spectral backend yields a finer velocity resolution than characterized HIPASS, making it possible to detect sources with HI line widths as narrow as $\sim 15 \text{ km s}^{-1}$. As discussed in Haynes et al. (2011) and earlier papers in the ALFALFA series, the median centroiding accuracy of the HI sources is $\sim 20''$ allowing the identification of most probable optical counterparts in 97% of cases. ALFALFA provides the first full census of HI-bearing objects over a cosmologically significant volume of the local universe (Martin et al. 2010) so that its population includes the very rare objects missing from the smaller volumes sampled by previous blind HI surveys. It enables the study of the characteristics of HI-selected galaxies in comparison with the galaxy populations included in the SDSS and GALEX surveys.

The 2011 ALFALFA catalog, ‘ $\alpha.40$ ’, covers $\sim 40\%$ of the final targeted sky area (Haynes et al. 2011), giving HI masses, systemic velocities and HI line widths for ~ 16000 high quality detections (§2.1). In addition to the HI line parameters, the $\alpha.40$ catalog also includes an assignment of the most probable optical counterpart (OC) to each HI line detection. Haynes et al. (2011) discuss the process of assigning OCs to the HI sources, and where the footprints of the surveys overlap, the HI sources are cross-referenced to the SDSS Data Release 7 (DR7: Abazajian et al. 2009), permitting the derivation of properties associated with the stellar components of the HI-bearing galaxies detected by ALFALFA. As shown by Haynes et al. (2011), the $\alpha.40$ population is highly biased against red-sequence objects.

In this paper, we investigate further the nature of the stellar counterparts of the $\alpha.40$ HI line detections, adding to the optical SDSS data photometric measures from the GALEX catalog (§2.2). By combining the measurements of the gaseous and stellar components, we characterize the $\alpha.40$ galaxy population and study in §3 global trends within it. SED-fitting to the seven bands from the UV to optical is applied to derive the principal stellar properties, including the stellar masses (§3.1) and SF (§3.2). To understand better the characteristics of the gas-bearing galaxies and the potential bias associated with HI-selection, we define a volume-limited sub-sample extracted from the $\alpha.40$ catalog with a similar one extracted from the SDSS-DR7 (§4.1) and compare the two in §4.2 in terms of survey depth (§4.2.1), extinction (§4.2.2), color (§4.2.3), SF behavior (§4.2.4), etc. The empirical distribution of the halo spin parameter is derived in §5, which suggests that the HI-selected galaxies favor high spin parameter halos. Our conclusions are summarized in §6.

Throughout this paper, we adopt a reduced Hubble constant

$h = H_0/(100 \text{ km s}^{-1} \text{ Mpc}^{-1}) = 0.7$. A Chabrier (2003) IMF is adopted.

2. SAMPLE AND DATA

2.1. ALFALFA parent sample

The HI parent sample used here is drawn from the $\alpha.40$ catalog presented in Haynes et al. (2011). The $\alpha.40$ catalog covers two regions in the Spring sky (i.e., the Virgo direction, $7^{\text{h}}30^{\text{m}} < \text{RA} < 16^{\text{h}}30^{\text{m}}$, $4^\circ < \text{Dec} < 16^\circ$ and $24^\circ < \text{Dec} < 32^\circ$) and two in the the Fall sky (i.e., the anti-Virgo direction, $22^{\text{h}} < \text{RA} < 3^{\text{h}}$, $14^\circ < \text{Dec} < 16^\circ$ and $24^\circ < \text{Dec} < 28^\circ$). As discussed in Haynes et al. (2011), ALFALFA HI line detections are categorized according to their signal-to-noise ratio (S/N) and corresponding reliability. Code 1 sources have $S/N \gtrsim 6.5$ and are highly reliable. Another set of entries, designated as “code 2” sources, or “priors”, have lower S/N but coincide with a likely OC at the same redshift. Most of these sources are likely to be real (Haynes et al. 2011). The catalog includes 15041 extragalactic HI sources, 11941 with code 1 and 3100 with code 2. In this paper, we consider both the code 1 and 2 $\alpha.40$ detections and adopt the HI measures, distances and HI masses presented in the $\alpha.40$ presented by Haynes et al. (2011). It is important to note that $\sim 70\%$ of the ALFALFA sources are new HI detections proving that previous targeted surveys based on optical selection (magnitude, size and morphology), most notably the extensive collection contained in the Cornell digital HI archive (Springob et al. 2005), missed large segments of the local gas-bearing population.

In particular, one of the most surprising results of ALFALFA to date is the richness of the high HI mass galaxy population (Martin et al. 2010). With its combination of sensitivity and depth, ALFALFA reveals that there still exists at $z \sim 0$ a population of massive galaxies which retain massive HI ($M_{HI} > 10^{10} M_\odot$) disks. Some, in fact, contain a dominant fraction of their baryons in HI gas. As the most HI massive local galaxies, they are the $z \sim 0$ analogs of the massive disks detected at $z \sim 0.2$ (Catinella et al. 2008) and those that will dominate the deep surveys being planned for even higher z with the EVLA, APERTIF, ASKAP and MeerKAT and eventually the Square Kilometre Array (SKA). By design, ALFALFA provides a census of HI bearing galaxies within a cosmologically significant volume over a wider dynamic range of HI masses than previous studies. It thus serves as the reference $z \sim 0$ HI-selected population.

2.2. Optical and UV counterparts of ALFALFA HI sources

In addition to the HI measurements, Haynes et al. (2011) attempt to identify the most probable optical counterpart (OC) of each HI line source in the $\alpha.40$ catalog. Ancillary information such as redshift coincidence, angular size, color and morphology is used in making the OC assignment. As discussed by Haynes et al. (2011), the process is not perfect, particularly for low signal-to-noise sources for which the centroiding accuracy can exceed $30''$ and in regions of source confusion. Nonetheless, the vast majority of OC assignments are probably valid and thus permit the comparison of the stellar and gaseous components of the ALFALFA population.

2.2.1. SDSS photometry

Towards this aim, Haynes et al. (2011) also provide a cross reference of the assigned OCs with the SDSS-DR7

(Abazajian et al. 2009) where the two surveys have overlapping sky footprints. The northern Fall region is not covered by the SDSS legacy imaging survey DR7. Of the 15041 HI source included in the $\alpha.40$ catalog, 201 have no OC assigned by Haynes et al. (2011), 2310 lie outside the DR7 footprint, and 60 appear to be in the region of the SDSS imaging survey but cannot be associated with an object in the SDSS photometric database. In most of the latter cases, the OC is evident in the SDSS images but is projected close to a bright foreground star or contaminated by its glare.

As discussed by numerous authors e.g., West et al. (2010), gas rich nearby galaxies are often blue and patchy with the result that their overall optical emission is shredded among several photometric objects by the SDSS pipeline measurements. The ALFALFA-SDSS cross-reference given in Table 3 of Haynes et al. (2011) includes a photometric code that identifies objects with suspicious SDSS photometry, and we exclude such objects (293/12470) from the SED-fitting. For the others, we require that model magnitudes are available in all five SDSS bands (u, g, r, i, z) and retrieve the SDSS photometric parameters from the standard SDSS-DR7 database.

The current $\alpha.40$ catalog used here relies on the optical identifications and photometry derived from the SDSS-DR7 database as cross-referenced in Table 3 of Haynes et al. (2011). Blanton et al. (2011) have presented a new method for background subtracting the SDSS imaging which they apply to the SDSS-III DR8 images. As ALFALFA progresses, we will migrate to use of the improved SDSS pipeline. Especially for purposes of comparison with results obtained by other authors who have likewise relied on DR7, we retain the use of DR7 in the present work.

2.2.2. GALEX photometry

Using a similar approach, we have conducted a separate cross-match of the ALFALFA OCs to the GALEX UV photometric catalog. The imaging mode of the GALEX instrument surveys the sky simultaneously in two broad bands, one in the FUV (effective wavelength of 1516Å) and a second in the NUV (effective wavelength of 2267Å). The GALEX field of view is $\sim 1.2^\circ$ in diameter (Morrissey et al. 2007), although image quality deteriorates in the outer annulus beyond a radius of 0.55° . We use the GALEX GR6 data release, with its improvements to flat fielding, adjustment to the photometric zero-point, etc. Given the poorer image resolution ($\sim 4.5''$ FWHM), compared to that of the SDSS, as well as the lower UV source density, visual inspection shows that the GALEX DR6 pipeline measurements corresponding to the ALFALFA galaxies suffer less from shredding issues. We have also validated that the GALEX pipeline photometry is in close agreement with our own photometric reprocessing of the GALEX images for a sample of dwarf galaxies detected by ALFALFA (Huang et al. 2012).

The GALEX mission includes several survey modes that differ in their exposure time per tile: The All-sky Imaging Survey (AIS) is the shallowest (~ 100 sec), while the Medium Imaging Survey (MIS, ~ 1500 sec) is designed to maximize the coverage of the sky that is included in the SDSS. The latter also includes the Nearby Galaxy Survey (NGS), a selected set of targeted fields of similar depth as the standard MIS. A third Deep Imaging Survey (DIS) is much deeper but covers only a small solid angle. In adopting the GALEX counterparts, we give preference to sources extracted from the MIS, NGS or DIS, but make use of the AIS for those objects not included

in the deeper surveys.

To cross-match the ALFALFA OCs to the GALEX catalog, we first search the position of the ALFALFA OCs for all GALEX neighbors within $36''$. Objects close to the GALEX field edge, i.e. with a distance from the field center $> 0.55^\circ$, are dropped to avoid duplications with objects in overlapping tiles and known GALEX imaging artifact effects. To permit homogeneous SED-fitting to all 7 bands ($FUV, NUV, ugriz$), we require that UV images of comparable depth must exist for both of the UV bands; this criterion results in the adoption of AIS measurements where the MIS catalog is incomplete, e.g. because of the failure of the FUV detector. In other cases, matches are missed because the FUV and NUV sources may fail to coincide because of, e.g. astrometry error or shredding in one or both bands. Among the 14840 extragalactic ALFALFA sources with OCs 1828 (12.3%) have no GALEX counterpart returned within $36''$, either because they lie outside of the GALEX footprint or have no detected UV emission in both bands. 516 (3.5%) are excluded because they lie too close to a GALEX field edge and 1317 (8.9%) are not matched because all neighbors are detected only in one band but not the other. The remaining 11179 OCs are matched to the nearest neighbor in the GALEX catalog with 7752 (52.2%) matched to UV sources found in the AIS and 3427 (23.1%) to ones in the MIS. The median separation between the coordinates of the OC and the cross-matched GALEX object is only $1.6''$.

Although the addition of the GALEX UV photometry sets better constraints on the SF properties and dust extinction (Salim et al. 2005), the requirement that UV sources must be detected in both bands introduces an additional bias against non star-forming galaxies. SED-fitting to the SDSS bands only (Huang et al. 2012) demonstrates that 13.5% of the 12156 galaxies in the $\alpha.40$ -SDSS DR7 cross-match have $\log SFR < 10^{-11} \text{ yr}^{-1}$, and therefore belong to the quiescent population. This fraction drops to 3.9% of the 9417 $\alpha.40$ galaxies that have counterparts in both the SDSS and GALEX photometric catalogs. As we discuss in §4, the HI-selection produces the stronger bias against the red sequence.

2.2.3. UV-to-optical colors of ALFALFA galaxies

Figure 1 presents the optical-UV color-color diagram derived for the 9417 galaxies which have complete entries in all three of the ALFALFA- $\alpha.40$, the SDSS-DR7 and GALEX-DR6 catalogs and for which the 7-band SED-fitting produces a valid result (see §3), denoted as the $\alpha.40$ -SDSS-GALEX sample hereafter. Contours and points depict the distribution for the $\alpha.40$ -SDSS-GALEX sample in high and low number density regions respectively, with typical error bars shown in the upper left corner (pipeline magnitude errors). Colors hereafter are all corrected for Galactic extinction but not internal extinction (see §4.2.2). In the optical, the SDSS pipeline extinction-corrected values are used, while at UV wavelengths, we adopt the $E(B - V)$ values based on the maps of Schlegel et al. (1998), the Cardelli et al. (1989) extinction law with $R_V = A_V/E(B - V) = 3.1$, and $A(\lambda)/E(B - V) = 8.24$ for the FUV and 8.2 for the NUV, following Wyder et al. (2007). Because of the bandwidth limit of ALFALFA, only low redshift galaxies with small K-correction are included, and we ignore this term in computing colors, i.e., no K-correction is applied.

Because it contrasts the recent SF, as indicated by the UV light, with the total past SF, as indicated by the optical light, the UV-to-optical color is a stronger diagnostic of SFH than colors derived from the optical bands only. This result is

also evident in Figure 1. Based on the distribution of their GALEX-SDSS matched catalog, Salim et al. (2007) define their blue cloud galaxies as those with $(NUV-r) < 4$. Using the same cutoff, 96% of the $\alpha.40$ -SDSS-GALEX galaxies lie on the blue side, suggesting that HI-selection induces a strong preference for blue star-forming galaxies, or conversely, a strong bias against red sequence galaxies. Bluewards of this division, the two colors are well correlated with a slope of $\delta(u-r)/\delta(NUV-r) \sim 0.6$, which is comparable to what was found by Wyder et al. (2007), $\delta(u-r)/\delta(NUV-r) \sim 0.5$. Although only a small population (411) of galaxies appear redward of $(NUV-r) = 4$, the $(u-r)$ colors of the red objects increase less quickly with $(NUV-r)$ and the distribution of the reddest tail is nearly flat. As discussed in §4.2.2 the degeneracy of $(u-r)$ among the red populations is even more pronounced in an optically-selected sample with more red galaxies. Therefore, the SED-fitting to the SDSS bands only is sufficient to constrain the SF for the HI-selected blue galaxy population in general (e.g. Huang et al. 2012) but gives systematic overestimates of SFRs for optically-selected red galaxies such as those in the Virgo cluster known to have quenched SF (e.g. Hallenbeck et al. 2012), i.e., it is crucial to include the UV bands in the SED-fitting to infer the SF of the red population. As a result, we adopt the UV-optical color $(NUV-r)$ rather than the optical-only $(u-r)$ in the analysis of SF and gas properties below.

3. GLOBAL PROPERTIES OF THE ALFALFA GALAXY POPULATION

To derive the global properties of the stellar components of the ALFALFA galaxies, we adopt the methodology of Salim et al. (2007). In particular, stellar masses and SFRs are derived from SED-fitting the seven GALEX/SDSS bands. Further details of the method and fitting quality as applied to the $\alpha.40$ sample are found in Huang et al. (2012) which focuses on the lowest HI mass dwarf population. In addition, the Gaussian prior distribution of the effective optical depth in V band, τ_V , is applied, with the mean predicted by Giovanelli et al. (1997) and a standard deviation of 0.55 dex. Such an improvement reduces the overestimate of internal extinction and SFR with decreasing stellar mass, as identified by Salim et al. (2007) (see §4.2.2 for more details), but still accounts for the effect of dust in disk systems. In this section, we discuss the results for the full $\alpha.40$ -SDSS-GALEX overlap sample (9417 galaxies).

3.1. Gas and stars

Current understanding interprets the standard SDSS color magnitude diagram (CMD) in terms of an evolutionary scenario under which galaxies migrate from the blue cloud to the red sequence as they assemble their mass. This picture is further reinforced by the presence of the star-forming sequence in the SSFR vs. stellar mass diagram; more massive galaxies show lower SSFRs. Consistent with this picture, one would expect galaxies to grow increasingly gas poor and thus having lower HI fractions f_{HI} (defined throughout this work as $f_{HI} \equiv M_{HI}/M_*$) as they assemble their mass. Therefore, blue galaxies with high gas fractions indicate disks which are stable against collapse, making their SF much less efficient (West et al. 2009).

3.1.1. HI versus stellar mass

In the last decades, many studies have investigated how the HI content varies with stellar properties in galaxies, such as

morphology, luminosity, size and SF activity (Gavazzi et al. 1996; Boselli et al. 2001; Kannappan 2004; Disney et al. 2008; Garcia-Appadoo et al. 2009; West et al. 2009, 2010; Toribio et al. 2011). Despite the complex interplay of dynamics, SF, chemical enrichment and feedback etc., the stellar and HI components, as well as the dark matter halo, exhibit correlations with each other. However, many of these studies have relied on relatively small and/or inhomogeneous samples limited to the very nearby universe. Although the main scaling relations were known, constraints on the accuracy of these relationships, as well as the quantification of their scatter are still not well determined. Based on an $H\alpha$ narrow-band imaging survey of ~ 400 galaxies selected from ALFALFA, Gavazzi et al. (2012a,b) also investigate the relationships between HI and newly-formed stars, emphasizing the study of environment effects. Here we focus on the nature of the population detected by the ALFALFA survey.

Figure 2 illustrates the relationships of the HI mass and f_{HI} (the vertical axes) with the stellar mass and color (horizontal axes). The contours and points outline the distributions of the galaxies in the $\alpha.40$ -SDSS-GALEX sample; the blue diamonds and solid lines trace the average values $\langle \log y \rangle$ and $\langle \log x \rangle$ in bins of $\log x$, with a bin size of 0.5 dex in panels (a), (c) and (d). The number of galaxies in each stellar mass or $(NUV-r)$ color bin is given at the bottom of panels (c, d). Typical error bars of individual galaxies are shown in the corners of panels (a) and (d). The Spearman's rank correlation coefficients of the relation, r_S , are shown in the upper right corner of all panels. Compared to similar studies that have previously probed the global scaling relations involving M_{HI} (e.g. Bothwell et al. 2009; Catinella et al. 2010), the $\alpha.40$ sample offers a more complete statistical sampling of the full range of HI and stellar masses. As discussed in Haynes et al. (2011), ALFALFA's combination of sensitivity, sky coverage and bandwidth yields a sample that probes a wide dynamical range in HI mass (7-11 dex with a mean of 9.56 dex), from the most massive giant spirals with $M_{HI} > 10^{10} M_\odot$ to the lowest HI mass dwarfs with $\log M_{HI} < 10^{7.5} M_\odot$. In fact, the stellar mass range that is probed is slightly wider: 6–11.5 dex, with a mean of 9.43 dex. As an HI-selected sample, $\alpha.40$ -SDSS-GALEX demonstrates the ability to recover galaxies with small M_* .

Figure 2(a) shows the distribution of M_{HI} with M_* . The cyan dash-dotted line traces the linear fit to the GASS sample of high stellar mass galaxies ($M_* > 10^{10} M_\odot$; Catinella et al. 2010):

$$\log\langle M_{HI}(M_*) \rangle = 0.02 \log M_* + 9.52.$$

Note that those authors chose to calculate $\log\langle M_{HI} \rangle$ rather than $\langle \log M_{HI} \rangle$ because the $\langle \log M_{HI} \rangle$ value is depressed by the contribution of gas-poor galaxies in their M_* -selected sample; a similar effect results in their adoption of $\log\langle f_{HI} \rangle$ rather than $\langle \log f_{HI} \rangle$. In contrast, an HI-selected sample such as ours does not sample the low HI fraction massive objects so that, as a function of $\langle \log M_* \rangle$, $\langle \log M_{HI} \rangle$ and $\langle \log f_{HI} \rangle$ adequately trace the main distribution. Moreover, as pointed out in Cortese et al. (2011), the distribution of f_{HI} is closer to log-normal than Gaussian, and thus they also prefer $\langle \log f_{HI} \rangle$ to $\log\langle f_{HI} \rangle$.

We confirm the previous findings that M_{HI} increases with M_* . However, the correlation does not appear to be a simple linear one, i.e. $\delta M_{HI}/\delta M_*$ is smaller at the high mass end.

The linear fit to the blue diamonds in Figure 2(a) is

$$\langle \log M_{HI} \rangle = \begin{cases} 0.712 \langle \log M_* \rangle + 3.117, & \log M_* \leq 9; \\ 0.276 \langle \log M_* \rangle + 7.042, & \log M_* > 9. \end{cases} \quad (1)$$

This trend is consistent with the idea that once AGNs are turned on in massive galaxies, gas is lost due to AGN feedback. The fact that f_{HI} is lower in massive SF/AGN composites than in purely SF galaxies of the same mass may be the cause of a similar break in slope of the star-forming sequence (see §3.2, at a slightly higher transition mass, $\log M_* \sim 9.5$). Furthermore, compared to the high stellar mass GASS galaxies, the ALFALFA population is overall more gas-rich for the same stellar mass ($\log M_* > 10$) and traces a steeper slope in the M_{HI} vs. M_* scaling relation, i.e. there is a systematically larger discrepancy in the typical HI content of the ALFALFA and GASS populations in the largest M_* bins. Besides the change in slope, there appears to be an increased scatter in the M_{HI} distribution below $\log M_* \sim 9$, a regime only poorly sampled by other studies. In fact, Huang et al. (2012) point out that at the lowest HI masses, ALFALFA detects a population of dwarf galaxies with low f_{HI} for their M_* ; some of these objects are dwarf ellipticals/spheroidals (dE/dSph) galaxies in the Virgo cluster and may have accreted their current gas supply only recently (Hallenbeck et al. 2012). The HI gas can be easily removed in low mass systems due to their shallow potential wells, so that the galaxy migrates onto the red sequence as its SF quenches.

Figure 2(c) shows how the HI fraction f_{HI} depends on M_* . The cyan dash-dotted line again traces the GASS result for the high stellar masses (Catinella et al. 2010), while the green (upper), red (lower) and yellow (middle) dashed lines trace the separate samples of HI-normal galaxies, ones in Virgo and outside-Virgo respectively from Cortese et al. (2011) who looked for trends among galaxies in different environments. Again, the known trend that higher M_* galaxies have lower f_{HI} is clearly evident, with a correlation coefficient $r_S = -0.85$. M_* depends more strongly on f_{HI} than on M_{HI} ($r_S = 0.71$) partly because the same measure of the M_* enters also in the computation of f_{HI} . Compared to other findings, the ALFALFA population uniformly includes galaxies which are more gas rich for a given M_* . Their extraordinarily high f_{HI} indicates little integrated past SF, while their blue colors may be attributed to a SFH that steadily rises to the present day or a truly young stellar component (Garcia-Appadoo et al. 2009).

Both the GASS and Cortese et al. (2011) samples include galaxies that have lower f_{HI} and lie below the ALFALFA HI detection threshold. For example, the Virgo cluster is well known to contain a significant population of HI deficient galaxies (Davies & Lewis 1973; Giovanelli & Haynes 1985; Solanes et al. 2002) whose HI line flux densities are too low for them to be detected by the short ALFALFA observations; their detections were made using longer duration, target Arecibo observations. The offset of the ALFALFA population from the other samples is therefore as expected. However, it is interesting to note that the scaling of f_{HI} with $\log M_*$ derived here and by Cortese et al. (2011) for the HI-normal galaxies, while they do not coincide in amplitude, do show comparable slopes at intermediate masses, and perhaps the same is true for all samples at $\log M_* < 9.7$. A “fast”, shallow survey like ALFALFA derives the same trend as one which relies largely on much deeper, pointed observations. The flattening off of f_{HI} at $\log M_* \lesssim 9$ is traced only by the ALFALFA dwarfs

(Huang et al. 2012).

It is important to note that the nearby, low mass galaxies are the ones most susceptible to shredding by the SDSS pipeline so that, statistically, their stellar masses are more likely to be underestimated, resulting in an extreme tail of galaxies with unrealistically high f_{HI} . By exclusion of objects with suspect SDSS photometry as noted by Haynes et al. (2011), the most egregious cases have been excluded from this analysis. Similar problems with the use of the SDSS pipeline measurements have much less effect on the main distribution. At the same time, source confusion within the ALFA beam (FWHM $\sim 3'.5$) is more likely among more distant systems so that the M_{HI} (and f_{HI}) of some high M_{HI} sources may be overestimated. However, other than cases of major mergers, the highest M_{HI} galaxies are always significantly more massive than their small companions, so that the change in f_{HI} , if the contribution from companions is removed, would only be small. Overall, the trend of falling f_{HI} with increasing M_* seen in the ALFALFA galaxies is well defined. For the ALFALFA population overall, the median $f_{HI} \sim 1.5$. HI-selected galaxies are uniformly gas rich for their stellar mass following a scaling relation over the range of *stellar mass* $8.0 < \log M_* < 11.0$.

In Figure 2(c), the number density of points drops sharply on the upper edge of the main distribution: there is a real cutoff in the galaxy population with even higher f_{HI} than ALFALFA detects. The increased dispersion in the contours on the lower edge of the f_{HI} distribution with substantial numbers of outliers with lower f_{HI} than the main population confirms that, because of its HI-selection, ALFALFA misses much of the gas-poor galaxy population. Longer integration times would obviously detect galaxies of lower M_{HI} and thus lower f_{HI} at constant M_* . The GASS observing strategy (Catinella et al. 2010) is specifically designed to probe to constant f_{HI} by conducting significantly longer but targeted HI observations. The GASS program thus characterizes the overall population of galaxies selected by stellar mass at the high mass end. The ALFALFA survey, on the other hand, samples well the full dynamical range of the HI-rich (for their stellar mass) population

Figures 2(b, d) explore the variation of M_{HI} and f_{HI} with $(NUV - r)$. Definitions of diamonds and lines in panel (d) are the same as in panel (c). As noted in Figure 1, nearly all ALFALFA galaxies are blue, and the population is highly biased against the red sequence. While there is a wide spread in M_{HI} , there is little trend of M_{HI} with color ($r_S = 0.28$). In fact, there are 128 $\alpha.40$ -SDSS-GALEX red galaxies ($NUV - r > 4$) with $\log M_{HI} > 10$, including the early type galaxies with quenched SF but unusually high HI masses (e.g. AGC 260442), the edge on galaxies with significant internal extinction (e.g. UGC 6312 has a dust lane evident in the SDSS image), and even the “red spirals” found in the Galaxy Zoo (Masters et al. 2010), e.g. UGC 9624 and UGC 9283. There are 116 red galaxies ($NUV - r > 4$) with $\log M_{HI} < 9.5$; most are early type “dead” galaxies. Cortese et al. (2011) found that the blue cloud galaxies have the same f_{HI} regardless of environment, whereas for the red galaxies, Virgo members are significantly gas poorer than HI-normal systems (see dashed lines in Figures 2d). In particular, their fit for HI-normal galaxies (green) agrees well with the main trend for the $\alpha.40$ galaxies.

In contrast, f_{HI} is a strong function of color among the ALFALFA population ($r_S = -0.79$ in panel d), at least among the blue cloud galaxies, i.e. the bluer galaxies tend

to have higher HI fractions. However, this trend gradually flattens for the very red galaxies ($NUV - r \gtrsim 3.5$), i.e. the very red galaxies among the ALFALFA population have higher f_{HI} than would be predicted by extrapolation of the trend traced by the blue galaxies. Compared to the f_{HI} vs. $(NUV - r)$ trends derived by Catinella et al. (2010) or Cortese et al. (2011), traced by the dash-dotted and dashed curves respectively in panel (d), the offset of blue diamonds on the blue side is small, but the deviation becomes systematically larger in the redder bins. Such a change in behavior can be partly explained by the fact that ALFALFA detects only a very small subset of these red galaxies. The presence of HI in this small population of otherwise ‘‘red and dead’’ galaxies is most easily explained if their HI gas has been acquired only recently, as has been invoked previously to explain the HI in ellipticals (e.g., Wardle & Knapp 1986; Morganti et al. 2006), and the annular HI distributions seen in many S0s (e.g., van Driel et al. 1988; Donovan et al. 2009). Deep HI synthesis imaging of the SAURON and ATLAS^{3D} samples of early-type galaxies shows that HI is commonly detected in galaxies which do not reside in cluster cores (e.g., Oosterloo et al. 2010; Serra et al. 2012). A significant fraction of non-cluster early-types contain some cool HI gas, with the large spread in HI content likely due to differences in their accretion histories.

3.1.2. Predictors of HI gas fraction

The tight correlation between f_{HI} and $(NUV - r)$ can be used as a predictor of M_{HI} given measures of color, i.e., the ‘photometric gas fraction’ technique (Kannappan 2004). Furthermore, a ‘fundamental plane’ of $f_{HI}-(NUV - r)-\mu_*$ has been identified by the GASS survey (Catinella et al. 2010), where the stellar mass surface density is defined as $\mu_* [\text{M}_\odot \text{kpc}^{-2}] = 0.5M_* [\text{M}_\odot]/\pi(r_{50,z} [\text{kpc}])^2$ and $r_{50,z}$ is the radius containing 50% of the Petrosian flux in the z -band. Their best fit ‘plane’ is

$$\log f_{HI} = -0.240(NUV - r) - 0.332 \log \mu_* + 2.856,$$

and the scatter of such a f_{HI} predictor is reduced relative to the $f_{HI}-(NUV - r)$ correlation with the additional parameter μ_* . Because colors essentially trace the SSFRs (see also §3.2), similar predictors are calibrated by Zhang et al. (2009) for an optically-selected sample as:

$$\log f_{HI} = \begin{cases} -1.25(g - r) - 0.54 \log \mu_* + 4.66; \\ 0.26 \log SSFR - 0.77 \log \mu_* + 8.53. \end{cases}$$

It should be noted that no correction for internal extinction is applied in those analyses, although it is well known that the inner disks of spirals are optically thick (e.g., Giovanelli et al. 1995). We discuss the need for an internal extinction correction below in §4.2.2. The f_{HI} predicted by these formulae are plotted on the horizontal axes in Figures 3(a-c), respectively. Compared to the ALFALFA measurements of the f_{HI} (vertical axes), they all predict systematically smaller f_{HI} . This reaffirms that the HI-selected sample is biased towards the gas rich population. The deviation from the one-to-one dashed line increases with f_{HI} in the case of the GASS calibration (Figure 3a). The Zhang et al. (2009) estimators (Figure 3b and c) systematically underpredict f_{HI} of the α .40-GALEX-SDSS galaxies by ~ 0.3 dex.

Exactly which scaling relation to use to predict the properties of a population depends of course on what the scientific objective is. For example, the scaling relations for an

optically-selected sample may be valid for a stellar mass selected population. However, the relations derived for ALFALFA give better predictions for the HI detection rate for future SKA surveys which will likewise be HI-selected. Previous simulations of SKA detection rate are mostly based on the HIPASS results locally (e.g., Abdalla & Rawlings 2005; Obreschkow et al. 2009). But HIPASS suffered from limitations in its volume sensitivity, and in fact, ALFALFA detects more HI sources at the high M_{HI} end (Martin et al. 2010). Based on the α .40-GALEX-SDSS galaxies, linear regression gives:

$$\begin{aligned} \log f_{HI} &= -0.25(NUV - r) - 0.57 \log \mu_* + 5.24; \quad (2) \\ &= -1.05(g - r) - 0.57 \log \mu_* + 5.12; \quad (3) \\ &= 0.27 \log SSFR - 0.64 \log \mu_* + 7.80. \quad (4) \end{aligned}$$

Note that for comparison with other authors, the colors used here are corrected for Galactic extinction but not for internal extinction. In Figures 3(d-f), the ALFALFA f_{HI} measures are plotted against the values predicted by equations (2)-(4), with the correlation coefficients $r_S = 0.88, 0.87$ and 0.87 respectively. The systematic offset is removed according to our best fit and the correlations are as tight as the Catinella et al. (2010) ($r_S = 0.88$) and the two different Zhang et al. (2009) ($r_S = 0.87$ and 0.86) results. Among the three planes, the $f_{HI}-(NUV - r)-\mu_*$ correlation has the least scatter and it is also tighter than the $f_{HI}-(NUV - r)$ correlation ($r_S = -0.79$).

Note that the fundamental plane found here is noticeably different from the GASS relationship (Catinella et al. 2010). The main trend in Figure 3(d) reveals a break in slope at $\log f_{HI} \sim -0.5$, whereas the GASS relation is confined to only below this critical f_{HI} . Although the GASS sample is complete in the massive M_* domain, it does not probe the lower stellar mass, gas rich systems. Blindly applying the fundamental plane defined by the massive gas-poor galaxies through extrapolation into the gas-rich regime results in serious underprediction of f_{HI} . Because of the change in slope, the deviation from (Catinella et al. 2010) is systematically larger in the high f_{HI} galaxies.

Because the HI population is so overwhelmingly dominated by blue cloud dwellers and since HI is presumably a constituent of a galaxy’s disk, not its bulge or halo, it seems appropriate to explore scaling relations which are tied more heavily to the galaxy’s disk. Hence, we define a disk stellar mass surface density $\mu_{*,r90} [\text{M}_\odot \text{kpc}^{-2}] \equiv 0.9M_* [\text{M}_\odot]/\pi(r_{90,r} [\text{kpc}])^2$, where $r_{90,r}$ is the radius containing 90% of the Petrosian flux in the r -band. Compared to $\mu_*, \mu_{*,r90}$ is based on the r -band flux with higher S/N and less bulge contribution. In addition, adopting colors corrected for internal extinction (see §4.2.2), we derive improved predictors as follows:

$$\begin{aligned} \log f_{HI} &= -0.17(NUV - r)_0 - 0.81 \log \mu_{*,r90} + 6.31 \quad (5) \\ &= -0.70(g - r)_0 - 0.79 \log \mu_{*,r90} + 6.16 \quad (6) \\ &= 0.22 \log SSFR - 0.78 \log \mu_{*,r90} + 8.03 \quad (7) \end{aligned}$$

The values given by equation (5)-(7) are plotted on the horizontal axes in Figures 3(g-i). They show less scatter from the one-to-one dashed line with better $r_S = 0.90$. We suggest that scaling laws which incorporate properties which reflect the disk nature of the HI distribution, and specifically the above relations, provide the most appropriate approach to predicting the characteristics of HI-selected populations.

3.1.3. Assessing the molecular gas H_2 contribution

ALFALFA is an extragalactic HI line survey and, as such, probes only the neutral ISM. Yet, the process of SF in most galaxies is more directly coupled to the molecular gas, and the question of which gas component – HI, H_2 or total gas – correlates best with SF is still debated. To account for the full gas content, we thus need to assess the expected contribution of molecular gas to the total gas mass in the ALFALFA population galaxies.

An outgrowth of the GASS survey of high stellar mass galaxies, COLD GASS is a legacy survey which has measured the CO(1-0) line of ~ 350 randomly selected GASS sample galaxies ($0.025 < z < 0.05$) with the IRAM 30m telescope. COLD GASS has uncovered the existence of sharp thresholds in galaxy structural parameters such as μ_* , concentration index and $(NUV - r)$ color, above which the detection rate of the CO line drops suddenly. These thresholds correspond approximately to the transition between the blue cloud and red sequence (Saintonge et al. 2011b). Even though Catinella et al. (2010) found some red sequence galaxies with a surprisingly large HI component, none of the 68 galaxies in the first installment of COLD GASS with $(NUV - r) > 5$ are securely detected in CO. At the same time, only 1.4% of the α .40-GALEX-SDSS galaxies have $(NUV - r) > 5$, so that the HI-selected galaxies should have a high detection rate in CO.

Under the assumption that molecular gas forms out of lower density clouds of atomic gas, one might naively expect a tight correlation between M_{HI} and M_{H_2} . However, within the subsample of galaxies detected both in HI and CO by COLD GASS, the fraction (M_{H_2}/M_{HI}) varies greatly, from 0.037 up to 4.09; the two quantities are only weakly correlated (Saintonge et al. 2011a). The relative proportions of molecular and dense atomic gas in giant molecular clouds depend on the cloud column density and metallicity (Krumholz et al. 2008), and the clouds could even be primarily atomic if the metallicity is sufficiently low (Ostriker et al. 2010).

Of all the parameters that Saintonge et al. (2011b) investigated, the mean molecular gas fraction ($f_{H_2} \equiv M_{H_2}/M_*$) among the COLD GASS galaxies correlates most strongly with their $(NUV - r)$ color, with

$$\log f_{H_2} = -0.219(NUV - r) - 0.596,$$

although it is weaker than the $f_{HI}-(NUV - r)$ correlation, probably because H_2 resides in the inner region where extinction is higher, whereas HI dominates in the outer disks (Saintonge et al. 2011a). At the same time, they find that f_{H_2} is only a weak decreasing function of M_* . As a result, although ALFALFA probes a lower stellar mass range than COLD GASS does, the $f_{H_2}-(NUV - r)$ correlation above can still be roughly applied to the α .40-GALEX-SDSS galaxies. Specifically, since the α .40-GALEX-SDSS galaxies have a mean $(NUV - r)$ of 2.24, the results of COLD GASS predict a mean f_{H_2} of 0.082 for the HI-selected population, higher than the 0.066 of the COLD GASS detections.

We note that although f_{H_2} is only a weak decreasing function of M_* , f_{HI} clearly decreases with increasing M_* , i.e., the M_{H_2}/M_{HI} fraction appears to decline in less massive galaxies (see also Blanton & Moustakas 2009). For luminous galaxies, a substantial fraction of the gas is sometimes in molecular form, but the detection of CO in low mass galaxies has been shown to be very difficult (e.g., Leroy et al. 2009). Therefore, we conclude that $f_{H_2} \lesssim 0.1$ for the ALFALFA

population and thus ignore its contribution to the total gas fraction, focusing instead on the well-determined atomic gas fraction f_{HI} .

3.2. Star formation properties

In addition to the stellar mass, SED-fitting also yields an estimate of the current SFR averaged over the last 100 Myr. Salim et al. (2005) have shown the importance of including the GALEX UV bands, especially the FUV, to reduce the uncertainties in SFRs derived from SED-fitting. In addition to the SFR itself, several other quantities of physical interest also become available. For example, the SSFR, defined as SFR/M_* , compares the current SFR with that in the past (as measured by M_*), and thus is well correlated with the birthrate-, or b - parameter, defined as $SFR/\langle SFR \rangle$. Both the SSFR and the b -parameter describe the SFH. At the same time, normalization of the SFR by M_{HI} instead of M_* yields the star formation efficiency (SFE), defined as SFR/M_{HI} . The SFE compares the current SFR with its potential in the future, the latter regulated by M_{HI} , the available fuel. The reciprocal of the SFE is the Roberts time, $t_R = M_{HI}/SFR$ (Roberts 1963; Sandage 1986), the timescale for depletion of the HI gas reservoir, assuming a constant SFR at the current level.

Figure 4 shows a montage illustrating how the SF related properties, SFR , $SSFR$, SFE (y axes) vary with M_* , M_{HI} and the $(NUV - r)$ color (x axes). As before, contours and Spearman's rank correlation coefficients are shown in the lower left corners of all panels. Typical error bars of individual galaxy estimates are plotted in the lower right corners of panels (a, e, i). In the bottom row, tracing the SFE, the cyan dashed line shows the average value obtained by Schiminovich et al. (2010) for the high stellar mass GASS sample, while the green dash-dotted line marks the value corresponding to the Hubble timescale.

3.2.1. The SFR and SSFR in HI-selected Galaxies

Among the ALFALFA population and in agreement with previous studies, e.g. Salim et al. (2007), SFRs generally increase but SSFRs decrease with increasing stellar mass (Figure 4a, d). Similar trends are also evident with M_{HI} (Figure 4b, e), albeit with larger scatter, especially in the $SSFR$ vs. M_{HI} distribution ($r_S = -0.31$). The trend of decreasing SSFR with increasing stellar mass suggests the “downsizing” scenario of structure formation (Cowie et al. 1996), such that the high M_* galaxies form most of their stars in the first ~ 3 Gyr after their formation (Bell et al. 2003) and today exhibit relatively suppressed SF. In contrast, the low mass systems in such a picture remain active in SF throughout their histories. Under a hierarchical dark matter halo assembly scenario in which the low mass structures form first and then merge to form massive galaxies, the “downsizing” concept suggests a late epoch of gas replenishment and regrowth in low mass systems.

Although an HI-selected sample like ALFALFA is biased against massive galaxies with low SFRs and low SSFRs (see also §4.2.4), there is a hint in Figures 4(a, d) that the number density of such galaxies increases in the $M_* \gtrsim 10^{10} M_\odot$ regime in comparison to the intermediate mass range ($10^8 M_\odot \lesssim M_* \lesssim 10^{10} M_\odot$). The presence of some points in the lower right corner of the SFR vs. M_* plot suggests that at least some objects with large stellar masses

and detectable HI but very low SFRs are included in the ALFALFA population. More importantly however, there is not a comparably rich population of massive HI disks with low SFRs, i.e., the number density of galaxies in the lower right corner of Figure 4b is lower than that in the lower right corner of 4a. Where there is a lot of HI, there is always some SF.

As evident in Figure 4(c), the expected correlation between SFR and $(NUV - r)$, that galaxies bluewards of $(NUV - r) \simeq 4$ have higher SFRs than ones redwards of that value (e.g. Salim et al. 2005), is not so well defined by the ALFALFA population ($r_S = 0.31$), mainly because ALFALFA detects only a few very red galaxies. In particular, we lack sufficient dynamic range in $(NUV - r)$ to probe the trend along the red sequence seen in optically-selected samples that galaxies bluer in $(NUV - r)$ have higher SFRs, especially if colors after extinction correction are plotted.

On the other hand, the $SSFR$ is a strong function of the $(NUV - r)$ color (Figure 4f), with the Spearman’s rank correlation coefficient $r_S = -0.76$. This is also the tightest among all the correlations shown in Figure 4. It is natural to expect that $(NUV - r)$ is closely tied to the $SSFR$. Since the NUV luminosity largely reflects the SF and the r -band luminosity the stellar mass, the $(NUV - r)$ color, as the ratio of the two, serves as a proxy for the $SSFR$. Given the fact that NUV better characterizes the SFR than the u -band, one may also expect the $SSFR$ to correlate better with $(NUV - r)$ color than with $(u - r)$. However, because NUV suffers more from internal extinction and the associated corrections can be highly uncertain, extra scatter is introduced when the NUV is used with accounting for the impact of extinction. In fact, as demonstrated in (§4.2.2) and Figure 8(b), a shift towards blue colors and an even tighter correlation between $SSFR$ and $(NUV - r)$ become apparent when extinction-corrected colors are used.

3.2.2. The star formation law in HI-selected galaxies

The underlying question linking gas to stars in galaxies, the “star formation law” (SFL), is what limits SF: the formation of molecular gas out of HI or the efficiency at which the available molecular gas is converted into stars (Schruba et al. 2011). Various forms of the SFL are studied, perhaps most common among them the empirical law describing how the SF surface density (Σ_{SFR}) is regulated by the gaseous surface density (e.g., Σ_{HI+H_2} in Kennicutt 1998).

It should be noted that since most galaxies are unresolved by the ALFA 3.5’ beam, ALFALFA measures only the global HI content. Our estimate of the SFL will thus be globally averaged. Numerous recent studies focusing on more detailed observations of smaller yet representative samples have demonstrated the regulation of SF by molecular gas. For example, the HI Nearby Galaxy Survey (THINGS; Walter et al. 2008) and the HERA CO Line Extragalactic Survey (HERACLES; Leroy et al. 2009) provide measurements of the surface densities of total gas, atomic and molecular gas, and SFR in \sim kpc-sized regions within a number of nearby galaxies. Measurements of the azimuthally averaged gas and SFR profiles show that the SFR correlates better with the molecular hydrogen component than with the total gas density within the optical disk (e.g. Bigiel et al. 2008), suggesting that the SFR is controlled by the amount of gas in gravitationally bound clouds and that H_2 is directly important for cooling. Krumholz et al. (2011a) collated observations of the relationship between gas and SFR from resolved observations of Milky Way molecular clouds, from kpc-scale observations of

Local Group galaxies, and from unresolved observations of both disk and starburst galaxies in the local universe and at high redshift. Those authors showed that the data are consistent with a simple, local, volumetric SFL and that the SFR is simply $\sim 1\%$ of the molecular gas mass per local free-fall time. Furthermore, Schruba et al. (2011) found a tight and roughly linear relationship between IR (inferring Σ_{SFR}) and CO (inferred Σ_{H_2}) intensity, with $\Sigma_{H_2}/\Sigma_{SFR} \sim 1.8$ Gyr. This relation does not show any notable break between regions that are dominated by molecular gas and those dominated by atomic gas, although there are galaxy-to-galaxy variations in the sense that less massive galaxies exhibit larger ratios of SFR-to-CO, an effect which may be due to depressed CO relative to H_2 in low metallicity galaxies. Similarly, Bigiel et al. (2011) demonstrated a roughly constant H_2 consumption time ($\Sigma_{H_2}/\Sigma_{SFR} \sim 2.35$ Gyr).

However, other works show that the relationship between SF and gas varies systematically depending on the local environment. Bigiel et al. (2010a,b), found an evident correlation between SF and HI in the outer disks of spirals and in dwarf galaxies where HI is likely to dominate the ISM. Given the poor correlation between HI and SFR found inside star-forming disks, this finding strongly hints that different physics governs the formation of star-forming clouds, and that the HI column is perhaps the key environmental factor in setting the SFR (Bigiel et al. 2010a). Furthermore, the SFL is likely to have a distinct form in the atomic-gas-dominated regime (e.g. $\Sigma_{SFR} \propto \Sigma_{HI+H_2} \sqrt{\rho_{sd}}$, theoretically by Ostriker et al. 2010, where ρ_{sd} is the midplane density of stars plus dark matter). Therefore, we may expect a steeper dependence of Σ_{SFR} on Σ_{HI+H_2} if there is a dropoff in the stellar and dark matter density with radius. There is no single universal slope predicted for the SFL in the diffuse-gas-dominated regime. In low gas surface density or low metallicity regions where gas is significantly atomic, thermal and chemical processes become dominant in determining where stars can form, and the gravitational potential of the stars and dark matter may have a significant effect. Similarly, the model developed by Krumholz et al. (2009b) suggests Σ_{SFR} becomes a steep function of Σ_{HI+H_2} when complexes of gas become primarily atomic, for low ISM surface density. Observations also confirm steeper slopes for the low density outer HI-dominated regions of spiral galaxies, as well as dwarf galaxies, compared to the inner molecular-dominated regions of spirals (Bigiel et al. 2010a).

The increasing SFR with HI mass evident in Figure 4(b) suggests the regulation of SF by the HI gas, with a correlation coefficient of $r_S = 0.71$. The red dash-dotted line in Figure 4(b) shows the linear fit to the α .40-SDSS-GALEX galaxies, with a slope of 1.19, suggesting a global, atomic, volumetric SFL. The close to unit slope indicates a SFE close to constant as a function of M_{HI} . The correlation between SFR and M_{HI} appears to be in conflict with the earlier finding that most galaxies show little or no correlation between Σ_{SFR} and Σ_{HI} (Bigiel et al. 2008). The high f_{HI} galaxies represented by the ALFALFA population appear to obey an unusual SFL which may not only depend on the H_2 , but also on the HI, stellar and dark matter properties. Additional observational and theoretical work is needed to evaluate how the SF efficiency of bound clouds depends on the relative amounts of cold HI versus molecular gas.

3.2.3. The SFE in HI-selected galaxies

Figures 4(g-i) illustrate the distribution of the SFE with M_* , M_{HI} and the $(NUV - r)$ color. The timescale for atomic gas depletion for the majority of the ALFALFA galaxies is shorter than the Hubble time t_H , and comparable to it for many of those with low stellar masses, $M_* < 10^9 M_\odot$.

For the high stellar mass GASS population, Schiminovich et al. (2010) found that, unlike the SSFR which decreases with increasing stellar mass, the SFE remains relatively constant with a value close to $SFE = 10^{-9.5} \text{ yr}^{-1}$, or equivalently $t_R \sim 3 \text{ Gyr}$. This value is longer than the molecular gas depletion timescale (see §3.2.2). Furthermore, those authors also found little variation in the SFE with stellar mass surface density μ_* , the $(NUV - r)$ color or the concentration index, a result which they interpreted as an indication that external processes or feedback mechanisms which control the gas supply are important for regulating SF in massive galaxies. Considering that $\log SSFR = \log SFE + \log f_{HI}$, an interesting implication of the weak correlation between the SFE and the stellar mass is that the fit to the $\log SSFR$ versus $\log M_*$ distribution would have a similar slope to that of the $\log f_{HI}$ vs. $\log M_*$, specifically -0.288 for $\log M_* \leq 9$ and -0.724 for $\log M_* > 9$ (see equations 1 in §3.1). However, the red dash-dotted line in Figure 4(d) shows the linear fit to the ‘star-forming sequence’ defined by the α .40-SDSS-GALEX galaxies:

$$\log SSFR = \begin{cases} -0.149 \log M_* - 8.207, & \log M_* \leq 9.5 \\ -0.759 \log M_* - 2.402, & \log M_* > 9.5. \end{cases} \quad (8)$$

The differences in the slopes suggest that $\langle SFE \rangle$ is a weak increasing function of $\langle M_* \rangle$ in the low M_* range but remains relatively constant above $\log M_* \sim 9.5$; this trend is also evident in the bottom row of panels ($r_S = 0.35$). The mild trend of increasing SFE with stellar mass seen in Figure 4(g) was not evident in the GASS study (Schiminovich et al. 2010) because the GASS sample includes only galaxies with $M_* > 10^{10} M_\odot$.

Rather than a simple continuous scaling relation, the change of slope given in equation (8) and evident in Figure 4(d), suggests that a transition mass exists at $M_* \sim 10^{9.5} M_\odot$ in the way in which star formation scales with total M_* . A similar transition mass at $M_* \sim 10^{9.4} M_\odot$ in SSFR is adopted by Salim et al. (2007) for their blue galaxies with $(NUV - r) < 4$. Those authors suggested that the lower SSFR is a consequence, at the high M_* end, of a population of systems which are both star-forming and have AGN, thereby yielding lower SSFRs than pure SF galaxies of the same mass. Similarly, Kannappan et al. (2009) identified a “threshold” stellar mass of several times $10^9 M_\odot$, below which the number of blue sequence E/S0 galaxies sharply rises. Those authors matched the threshold to the mass scale below which the mean HI content of low- z galaxies increases substantially both on the red sequence and within the blue cloud. Abrupt shifts in the SFE and gas richness near the “threshold mass” have been linked to the interplay of gas infall, supernova-driven winds, and changes in mass surface density. However, it is important to note that such a threshold falls below the “transition” mass characteristic of the “green valley”, identified in the, e.g., f_{HI} versus M_* and μ_* relations, at a stellar mass $M_* \sim (2 - 3) \times 10^{10} M_\odot$ proposed in many other works (e.g. Kauffmann et al. 2003; Baldry et al. 2004; Bothwell et al. 2009; Catinella et al. 2010) and suggested to be indicative of the SF quenching in massive galaxies as they migrate from the blue cloud to the red sequence.

Perhaps surprisingly, the ALFALFA galaxies have on average lower SFE, or equivalently, longer t_R , compared to the optically-selected population, with a mean of $SFE = 10^{-9.95} \text{ yr}^{-1}$, or equivalently $t_R = 8.9 \text{ Gyr}$, compared to the $t_R \sim 3 \text{ Gyr}$ derived for the GASS galaxies. We note that the average t_R value was volume corrected in Schiminovich et al. (2010), but not in Figure 4(g-i). However, we confirm that the volume correction (see §4.1) results in only subtle changes in the mean t_R as a function of M_* for the α .40-SDSS-GALEX galaxies, and it is still longer than $t_R \sim 3 \text{ Gyr}$. As we demonstrate in §4.2.4, the HI-selected galaxies have, on average, higher SFRs at a fixed stellar mass, so that the lower SFEs must result from their higher HI masses rather than from less active states of SF. This result reaffirms the general conclusion that HI-selected samples are strongly biased towards the most gas-rich galaxies. In agreement with the low SFEs characteristic of the ALFALFA population, Bigiel et al. (2008) have seen a decrease in SFE in the HI-dominated THINGS galaxies. Furthermore, Bigiel et al. (2010a) found that the SFE decreases with galactocentric radius among the THINGS sample across the outer disks beyond the optical radius, where HI dominates the ISM, with t_R well above Hubble time. In the THINGS dwarf galaxies, the contribution of H_2 to the total gas budget is generally small even in the inner disks, also corresponding to a low SFE (Bigiel et al. 2010a). All these results are consistent with the conclusion that SFEs are low, on average, in HI-rich systems.

However, we note that the low HI SFE may not be in conflict with the usual H_2 SFL. The HI-selected high f_{HI} galaxies may still follow the normal behavior of how stars form from H_2 , but rather that a bottleneck exists in the process by which star-forming molecular clouds assemble. The conversion of HI to H_2 depends on environment inside a galaxy and the relative abundance of HI and H_2 is key to setting the SFR (Bigiel et al. 2010b). Although the low HI SFE suggests the inefficiency of HI-to- H_2 conversion, the HI-to- H_2 ratio cannot be arbitrarily high. Ostriker et al. (2010) assumed an equilibrium state, in which cooling balances heating and pressure balances gravity. This balance can be obtained by a suitable division of the gas mass into star-forming (gravitational bound) and diffuse components such that their ratio is proportional to the vertical gravitational field. If too large a fraction of the total surface density is in diffuse gas, the pressure will be too high while the SFR will be too low. In this situation, the cooling would exceed heating, and mass would drop out of the diffuse gas component to produce additional star-forming gas.

Close examination of the SFE vs. M_* diagram in Figure 4(g) also reveals a considerable number of outliers with relatively high SFE at the high M_* end, falling well above the main distribution. In general, high SFEs have been measured in starburst galaxies and interacting systems which are consuming their gas reservoirs on very short timescales. However, a close inspection of 13 α .40-SDSS-GALEX galaxies with $\log SFE > -8$ shows that 9 of them are members of the Virgo Cluster. Ram pressure stripping results in strong HI deficiency and very short t_R in these extreme outliers. In contrast, the outliers below the main distribution can either be red, massive, low SSFR galaxies against which ALFALFA is strongly biased, or abnormally gas rich (for their stellar mass) but quiescent ones. The latter include candidates of recent re-accretion or systems in which the HI gas is somehow inhibited from forming stars. We return to this point in §5.

Figures 4(h, i) illustrate that the SFE barely changes with

either M_{HI} or color ($r_S = 0.03$ and 0.18 respectively) and the scatter in both correlations is large.

3.2.4. Linking the gas fraction f_{HI} to SF

As first discussed by Roberts (1963), it is not surprising that SF appears to be regulated by gas content. We have already argued that the $\log SSFR$ vs. $\log M_*$ diagram (Figure 4d) is similar to the $\log f_{HI}$ vs. $\log M_*$ one (Figure 2c), both showing similar slopes along the main trend; the distributions of $\log SSFR$ and $\log f_{HI}$ in given stellar mass bins also become broader at both the high- and low- mass ends. Hence, the star-forming sequence in the former diagram can also be understood as a sequence of gas-depletion in the latter one.

Previously, Kannappan (2004) also linked the f_{HI} to bimodalities in galaxy properties. She suggested that the bimodality in SFHs may be intimately related to changes in f_{HI} , and the transition in SF modes at $M_* \sim (2 - 3) \times 10^{10} M_\odot$, found by those authors, is not a cause but an effect of changing f_{HI} , as predicted in cold-mode accretion scenarios. Figure 5 illustrates these relationships by showing the averaged $\log f_{HI}$ of galaxies which lie in different loci in the CMD (left panel) and the $\log SSFR$ vs. $\log M_*$ diagram (right panel). Contours indicate the number density within the $\alpha.40$ -SDSS-GALEX sample in each grid point in the map, while the shade scale traces the mean HI fraction, $\langle \log f_{HI} \rangle$. As mentioned in §2.2.3, 96% of ALFALFA galaxies lie on the blue side of the optical-NUV CMD, whereas a smaller fraction (84%) lie on the blue side of an optical-only CMD (see §4.2.3 below). Some of this difference can be attributed to the greater impact of shredding on the SDSS pipeline magnitudes relative to that of the GALEX photometry. Because of the color gradient of galaxies (outer disks are bluer), the shredded central redder object is identified as the OC. As a result, the adopted photometric object may be redder in $(u - r)$ than the galaxy as a whole actually is. Moreover, the u -band is not as sensitive and thus yields photometry with large uncertainties for some of the galaxies. Additionally, the $(NUV - r)$ color is a stronger diagnostic of the SFH. For similar reasons, the $\langle \log f_{HI} \rangle$ of grid points in regions of low number density should be interpreted with caution. However the general trends (1) that the red-sequence is associated with low f_{HI} and (2) that blue cloud galaxies are gas rich are clearly evident. At a given M_r , redder $(NUV - r)$ colors, on average, indicate lower f_{HI} . Furthermore, such a variation of f_{HI} along the $(NUV - r)$ axis is more evident in the fainter M_r range: $\delta \langle \log f_{HI} \rangle / \delta \langle NUV - r \rangle \simeq 0.75$ at $M_r \simeq -16$, whereas $\delta \langle \log f_{HI} \rangle / \delta \langle NUV - r \rangle \simeq 0.25$ at $M_r \simeq -22$. Therefore, the correlation of $(NUV - r)$ and f_{HI} at a given M_r is hard to see in a sample with only massive galaxies, e.g. GASS (Wang et al. 2011).

Similarly, the right panel of Figure 5 illustrates how the HI fraction varies in the M_* -SSFR plane. As galaxies assemble their stellar mass and evolve along the star forming sequence, represented by the contours of high number density, their HI fractions decrease. In addition, for fixed M_* , galaxies with lower SSFRs have, on average, lower f_{HI} . Again this is more clearly evident at the low stellar mass end, and is consistent with the broadening in both the f_{HI} and $SSFR$ distributions at low M_* (Huang et al. 2012). In contrast, the variation of $\langle \log f_{HI} \rangle$ along the $\log SSFR$ axis at a given M_* is less evident for galaxies with $M_* \gtrsim 10^{9.5} M_\odot$. These two trends suggest that, for low M_* systems, high f_{HI} galaxies are more likely to be starburst galaxies (defined as high SSFR galaxies),

whereas galaxies in the high M_* regime selected by high f_{HI} are less likely to be starbursts. In summary, Figure 5 clearly demonstrates that the color, SF and gas evolution of galaxies are closely related to one another, as expected. Moreover, the regulation of SF by M_{HI} is stronger in the less massive galaxies.

4. THE IMPACT OF OPTICAL VERSUS HI-SELECTION

Future surveys of HI in galaxies at intermediate to high redshifts that will be enabled by the next generation of centimeter-wavelength radio telescopes (e.g. the SKA) will aim to infer the gas evolution from high redshift populations to the local well-studied ones. It is important therefore to understand the fundamental properties of local HI-selected galaxies, as represented by the ALFALFA catalog, and their biases relative to the overall galaxy population. In §3, we examined the global properties of gas, stars and SF within the ALFALFA galaxies themselves. They form an HI-rich, blue and less evolved population with low SFE; these characteristics are more pronounced in lower mass systems. M_{HI} and f_{HI} are linked to the SF related quantities, demonstrating the role that HI plays in the regulation of galaxy evolution along the star forming sequence. To understand how the HI-selected population is biased relative to ones selected by stellar mass or optical flux, in this section we construct samples from both the $\alpha.40$ and SDSS catalogues and then compare their similarities and differences.

4.1. Construction of control samples

In order to ensure the galaxies contained in each of the optically- and HI-selected samples are both representative of their respective population and fair enough to permit comparison with the other, we construct subsamples of both $\alpha.40$ and the SDSS in the same sky volume within their common footprint. The volume-limits imposed are similar to those discussed by Martin et al. (2010). Comparable selection criteria are applied with a further requirement that acceptable GALEX pipeline photometry must also be available, so that stellar masses and star formation properties can be derived robustly via SED-fitting.

4.1.1. ALFALFA selected sample, S_{HI}

As discussed by Martin et al. (2010), radio frequency interference from the San Juan airport FAA radar transmitter at 1350 MHz makes ALFALFA blind to HI signals in a spherical shell ~ 10 Mpc wide centered at a distance of ~ 215 Mpc. Therefore, as did those authors, we exclude 568 galaxies of the sample presented in §3 which lie beyond 15000 km s^{-1} (D_{sur} hereafter). To maximize the overlap of contiguous sky coverage between the current ALFALFA and SDSS DR7, we consider only the two regions in the northern Galactic hemisphere ($8^{\text{h}}00^{\text{m}} < \text{RA} < 16^{\text{h}}30^{\text{m}}$, $4^\circ < \text{Dec} < 16^\circ$ and $7^{\text{h}}40^{\text{m}} < \text{RA} < 16^{\text{h}}40^{\text{m}}$, $24^\circ < \text{Dec} < 28^\circ$, see Figure 6c). Applying these restrictions yields a sample within a sky volume of $V_{sur} = 1.987 \times 10^6 \text{ Mpc}^3$, a sky area of 1989 deg^2 and including 7638 $\alpha.40$ -SDSS-GALEX galaxies.

Next, a weight, V_{sur}/V_{max} , is assigned to each galaxy, where V_{max} is given by the maximum distance, D_{max} , at which an HI source can be detected by ALFALFA, if $D_{max} < D_{sur}$, with $V_{sur}/V_{max} = 1$ for the galaxies which can be detected all the way outwards to the D_{sur} . Because the ALFALFA sensitivity depends not only on the integrated HI line flux density, S_{int} [Jy km s^{-1}], but also on the HI line profile width, W_{50} [km s^{-1}], specifically, the fit to S_{lim} , the

limiting integrated HI line flux density that can be detected at S/N above 4.5 (code 1 and 2, 25% complete), as given in Haynes et al. (2011), is:

$$\log S_{lim} = \begin{cases} 0.5 \times \log W_{50} - 1.11 - 0.202, & \text{if } \log W_{50} < 2.5; \\ 1.0 \times \log W_{50} - 2.36 - 0.202, & \text{if } \log W_{50} \geq 2.5. \end{cases}$$

Then, D_{max} can be calculated given S_{lim} and M_{HI} , based on the standard equation $M_{HI} = 2.356 \times 10^5 D_{Mpc}^2 S_{int}$. In order to characterize the stellar component of the galaxies, we also perform a cross-match to the SDSS and GALEX databases. The application of such a weight scheme, or volume correction, is equivalent to resampling the galaxies by their HI properties (M_{HI} and W_{50}) alone, thereby reemphasizing the impact of HI-selection.

To further trim the sample, we drop galaxies whose weight $V_{sur}/V_{max} > 60$, i.e., we consider only galaxies that could be detected in more than 1.67% of the survey volume. This cutoff corresponds approximately to a lower M_{HI} limit of $\sim 10^{8.2} M_{\odot}$ (see Figure 6). There is not a hard M_{HI} cutoff because W_{50} also plays a role. The galaxies with $V_{sur}/V_{max} > 60$ are all relatively nearby ($D_{max} < 54.7 \text{ km s}^{-1}$, or assuming Hubble flow, $cz_{max} < 3829 \text{ km s}^{-1}$, $z_{max} < 0.0128$), and are low HI mass galaxies less representative of the survey overall. Further motivations for applying such a weight cutoff include: (a) for these very local sources, distance dependent quantities, e.g. M_{HI} , have large uncertainties due to their peculiar velocities; (b) such galaxies are also underrepresented in the SDSS redshift sample (see below); (c) for resolved, patchy dwarf systems especially, the SDSS pipeline magnitudes can suffer from shredding. The lowest HI mass systems have been considered separately in Huang et al. (2012).

The final HI-selected sample referred to as S_{HI} includes 7157 galaxies.

4.1.2. SDSS selected sample, S_{opt}

To construct an optically-selected control sample out of the same sky volume, V_{sur} , we queried the SDSS DR7 in the same RA and Dec ranges for photometric objects which have valid model magnitudes and were also spectroscopic targets. We also require them to (a) have a spectral classification of “galaxy”; (b) have an SDSS redshift, z_{SDSS} , determined with high confidence; (c) lie within the same redshift range as S_{HI} , $cz_{SDSS} < 15000 \text{ km s}^{-1}$; (d) have Galactic extinction-corrected r -band model magnitudes brighter than 17.77. 24379 galaxies meet these criteria. Note the redshifts adopted for this sample use the SDSS measurement, whereas that for the S_{HI} comes from the HI line measures. Given the cz_{SDSS} and coordinates, distances are estimated in the same manner as for the $\alpha.40$ sample using a local flow model for $cz < 6000 \text{ km s}^{-1}$, and Hubble distance otherwise (Haynes et al. 2011). Following the same procedure as for S_{HI} , we searched for GALEX cross-matches, and applied similar SED-fitting to the UV/optical bands.

To match the weight cutoff of the HI-selected S_{HI} sample, we also calculate weights for the SDSS-selected sample but here according to their optical fluxes. In this case, D_{max} is the maximum distance at which the object, given its r -band flux, could be included in the SDSS main galaxy redshift sample. As for the HI-selected sample, we drop galaxies with weights greater than 60. Given the magnitude limit of the SDSS redshift survey ($m_r < 17.77 \text{ mag}$), such a weight cut directly corresponds to an r -band absolute magnitude limit of $\sim -16 \text{ mag}$. Furthermore, since the mass-to-light ratio varies only

mildly with color, the luminosity cut approximately translates to a stellar mass lower limit of $\sim 10^{7.6} M_{\odot}$. Finally, a small number of galaxies are removed because they are included in the $\alpha.40$ catalog but have been previously noted by individual inspection to have suspect photometry (Haynes et al. 2011). The final optically-selected sample referred to as S_{opt} includes 16817 galaxies, of which 34% are cross-matched to the $\alpha.40$ catalog (see §2.2). The remainder are missed by ALFALFA either because they are (1) gas poor, (2) lie at a sufficient distance that their HI line flux densities falls below the HI sensitivity limit, or (3) for some other reason, e.g. their HI spectrum is contaminated by RFI or was not sampled at all (small gaps in ALFALFA coverage), or they correspond to one “child” of a shredded photometric parent object, but another photometric child is favored as the best match to the ALFALFA detection.

We note that the distributions of weight, V_{sur}/V_{max} , for both the samples highly peak at 1, and that the weight cut of 60 applied to each dataset is confirmed to be high enough to retain the main populations. Especially for the S_{opt} , 69% of the galaxies have a unit weight, i.e. can be detected outwards to the edge of V_{sur} as we defined here. The number of galaxies in bins associated with a weight above 1 drops more rapidly among the S_{opt} sample, confirming that the SDSS is deeper than ALFALFA.

4.2. Comparison of control samples

4.2.1. Basic properties

Figure 6 illustrates the comparison of quantities relevant to sample selection between the S_{HI} and the S_{opt} populations. In panels (a-c), red points denote galaxies in S_{opt} , whereas blue points denote galaxies in S_{HI} . In the histograms, red lines illustrate the distribution of S_{opt} and blue lines trace S_{HI} ; above each histogram, separate panels show the fraction of S_{opt} galaxies that are cross-matched to $\alpha.40$ in each bin. The numbers in each subset are indicated in panels (a) and (b).

The top row contains two Spaenhauer diagrams showing, respectively, the r -band absolute magnitude (panel a) and HI mass (panel b) versus distance. The solid vertical line represents the cz cutoff, 15000 km s^{-1} . We use the SDSS redshifts to derive distances for the S_{opt} and ALFALFA HI velocity for the S_{HI} . As discussed also by Martin et al. (2010), a survey must sample sufficient volume to detect very massive galaxies in either stellar (panel a) or HI (panel b) mass. ALFALFA for the first time provides a full census of HI-bearing objects over a cosmologically significant volume of the local universe.

As evident in Figure 6(a), SDSS is volume limited to $M_r \sim -19 \text{ mag}$. The sharp lower edge of the S_{opt} distribution above $D \sim 60 \text{ Mpc}$ results from the magnitude limit of the SDSS main galaxy redshift sample; as noted before, the adopted weight cutoff corresponds to $M_r \sim -16 \text{ mag}$ (horizontal dashed line). Since no limit on any optical quantity is applied to the S_{HI} subset, many blue points from $\alpha.40$ show up faintwards of the lower edge of S_{opt} , as faint as $M_r \sim -14$. We note that the blue points lying faintwards of the lower edge of S_{opt} and above $D \sim 60 \text{ Mpc}$ are still detected by the SDSS, but most often only as photometric objects; hence their optical redshifts are generally unknown. To enable SED-fitting however, all the S_{HI} galaxies are required to be detected in the SDSS; the very rare “dark” HI clouds without identified OCs included in $\alpha.40$ are outside the scope of this work and are not included in this discussion.

Figure 6(b) shows how M_{HI} increases with distance. The HI measures of S_{opt} all come from the $\alpha.40$ catalog (5653 out of 16817 S_{opt} galaxies, i.e., a cross-match rate of 34%). The weight cutoff applied to the S_{HI} sample results in an approximate limit of $M_{HI} \simeq 10^{8.2} M_{\odot}$ (horizontal dashed line). The red points below $10^{8.2} M_{\odot}$ are still detected by $\alpha.40$, but are excluded from the S_{HI} simply because of their high weights. Because of the way distances are derived (Haynes et al. 2011) from the observed redshifts, an insignificant difference (0.1 Mpc) of the median distance arises for the same galaxies in the S_{opt} - S_{HI} overlap sample. This difference is mainly due to the fact that the S_{HI} galaxies may be assigned membership in group whereas such information has not been applied to the S_{opt} sample. A few red outliers below the main distribution indicate objects without robust SDSS redshifts.

Panel (c) shows the sky distribution of the two samples. Besides the large scale structure, the required availability of GALEX photometry also contributes to the pattern. For example, the Virgo region is densely covered by at least MIS level visits, whereas the patches of sky blank in either sample and with regular edges arise from the lack of GALEX coverage in FUV and/or NUV. The distribution of distance is shown in panel (d). The two samples roughly coincide within ~ 100 Mpc. Above the histogram, the fraction of the S_{opt} galaxies that are cross-matched to $\alpha.40$ is shown. The first peak in number density coincides with the Virgo cluster (~ 16.5 Mpc), where S_{opt} clearly out numbers S_{HI} . Since the two distributions agree with each other again at larger distances ~ 50 Mpc, the disagreement at the Virgo distance indicates a real underdensity of gas-rich detections in S_{HI} , reflecting the well-known HI deficiency (Davies & Lewis 1973; Giovanelli & Haynes 1985; Solanes et al. 2002). Beyond ~ 100 Mpc, S_{opt} significantly overtakes S_{HI} , though the shapes of peaks or gaps still agree. This suggests that ALFALFA is capable of detecting HI massive objects at large distances, although the survey is not as deep as SDSS. Although in a given distance bin, the least massive objects contained in S_{HI} are even fainter than those in S_{opt} (i.e., the blue points below the lower edge of red distribution in panel a), ALFALFA is not as complete as SDSS at large distances.

The distributions of M_r for both samples are shown in panel (e). The vertical solid line denotes the equivalent weight cut applied to S_{opt} . While S_{opt} peaks at a slightly fainter M_r than S_{HI} , the two samples probe a similar M_r range so that their comparison is valid.

The distributions of axial ratio, given by the SDSS pipeline measures of the exponential fit a/b in r -band, are shown in panel (f). Because the ALFALFA sensitivity depends on the HI line profile width (see §4.1), S_{HI} might be expected to be biased against edge-on galaxies with high a/b values. For example, West et al. (2010) demonstrated that their Parkes Equatorial Survey (ES, a search through HIPASS cubes; Garcia-Appadoo et al. 2009) – SDSS common sample is slightly biased towards face-on galaxies, relative to an SDSS DR4 sample, with the mean $\log a/b$ equal to 0.17 and 0.21 for their ES–SDSS and DR4 samples respectively. However, panel (f) shows no such obvious bias. Both S_{HI} and S_{opt} have the same $\langle \log a/b \rangle = 0.28$. Furthermore, the cross-match rate even slightly rises for high a/b galaxies, with only a mild drop in the very last bin. Visual inspection shows that shredding can cause large errors in the a/b measures by the SDSS pipeline. The S_{opt} sample contains more galaxies with bulges making their a/b values appear to be smaller; in contrast, S_{HI} is biased against such galaxies.

4.2.2. Internal extinction in HI-selected galaxies

Previously, and in many analyses of SDSS derived samples, internal extinction is ignored. However, while the outer parts of galaxy disks are transparent, it is well established that the inner regions are optically thick at short wavelengths. Therefore, the neglect of internal extinction in disk-dominated galaxies is likely to introduce systematic inclination-dependent effects. In this section, we discuss (a) how internal extinction varies with stellar mass, (b) how internal extinction may introduce scatter into relationships involving colors and (c) how the extinction characteristics of the S_{HI} HI-selected galaxies compare to those derived from an optically selected sample S_{opt} . In the three figures associated with this section, Figure 7 - 9, typical error bars on individual points are plotted in selected panels in as well as the Spearman’s rank correlation coefficients.

Estimates of internal extinction are derived from UV/optical SED-fitting as before. The two-component dust model (Charlot & Fall 2000) is incorporated into the construction of the library of model SEDs (Gallazzi et al. 2005); the process accounts for both the diffuse interstellar medium (ISM) and short-lived (10 Myr) giant molecular clouds. Such estimates have overall larger uncertainties among the red-sequence galaxies relative to the blue cloud ones (e.g. Saintonge et al. 2011b), and contribute to the SFR uncertainties. Furthermore, Salim et al. (2007) identified differences between the effective optical depth in V band, τ_V , derived from emission-line fitting and that derived from SED-fitting, as a function of stellar mass. Specifically, at lower masses, the SED-fitting-derived value is systematically higher than the line-fitting-derived one, but the situation is reversed at the high mass end. Therefore, we applied a Gaussian prior distribution of τ_V for each model, given the absolute magnitude and axial ratio of the individual galaxies (see §3). The mean of the prior distribution is given by equation (12) in Giovanelli et al. (1997), which depends on the axial ratio and absolute magnitude, i.e. more luminous edge-on galaxies have larger extinctions.

Figures 7 (a-c) show plots of r -band internal extinction versus stellar mass for the S_{HI} galaxies. Despite the large uncertainty, internal extinction is a weakly increasing function of M_* in all these panels. Panel (a) shows SED-fitting-derived values before the prior distribution applied. A population of low mass red galaxies have unrealistically high A_r (SED no prior), because of the age-extinction degeneracy. The mean of the prior distribution of internal extinction, A_r (prior), is in panel (b). Although the A_r (prior) values of low mass galaxies are confined to low values, a population of massive galaxies have unrealistically low A_r (prior) likely due to the underestimate of a/b . Visual inspection shows that shredding tends to describe sources as rounder in edge-on galaxies; dominant bulges, dust lanes and seeing effects will also lead to systematic underestimates of the axial ratio. Panel (c) plots the SED-fitting-derived values after the prior distribution is applied, A_r (SED with prior). Both a lack of high mass galaxies with low A_r as well as of low mass ones with high A_r are evident in panel (c). Combining the distributions in panel (a) and (b), the A_r (SED with prior)– M_* correlation is the tightest of the three, with a correlation coefficient $r_S = 0.33$. Whereas applying the prior reduces the systematic offsets of the A_r estimates by SED-fitting, as well as the SFR values, it has little effect on the stellar mass values (Huang et al. 2012). Figure 7 (d) demonstrates that, as expected, the derived values

of A_r (SED with prior) are higher in more edge-on galaxies. Neglect of corrections for internal extinction will lead to the systematic underestimate of luminosity, so that hereafter we apply the SED-fitting with prior corrections.

For the subset of the S_{HI} galaxies (6164/7157) which are included in the MPA-JHU DR7 release of SDSS spectral measurements (<http://www.mpa-garching.mpg.de/SDSS/DR7/>, Brinchmann et al. 2004), we have verified that at $M_* \lesssim 10^{10} M_\odot$ the A_r inferred from the Balmer decrement and from the SED fitting using an A_r prior are in good agreement and the offset observed in Salim et al. (2007) is reduced. Above this mass the Balmer decrement leads to larger A_r values, but this is not unexpected as the SDSS spectra observe only a small region, typically towards the center of the galaxy where metallicities and dust attenuations are higher.

Another way to explore the importance of extinction correction in a population involves examining the scatter in the $\log SSFR - \text{color}$ diagram, as shown in Figure 8. Results for individual points (unweighted) for the S_{opt} sample are shown in the left panels and for the S_{HI} galaxies on the right, using the colors $(NUV - r)_0$ in the top row and $(u - r)_0$ in the bottom, respectively. The subscript ‘0’ in the labels indicates that the colors are corrected for internal extinction. As demonstrated in §3.2, $SSFR$ is an intrinsically strong function of $(NUV - r)$, because NUV traces the SFR and the r -band luminosity is related to the stellar mass. For the HI-selected population, comparison can be made directly of the volume-limited S_{HI} sample shown in Figure 8(b) with the corresponding result, uncorrected for internal extinction, shown in Figure 4(f) for the full α .40-SDSS-GALEX. As evident by inspection, in addition to a shift bluewards of the points in Figure 8(b), the dispersion about the mean relation is greatly reduced when the extinction correction is applied, and the Pearson correlation coefficient likewise improves from $r_P = -0.78$ to $r_P = -0.86$. This analysis indicates that the scatter in Figure 4(f) is substantially amplified by the lack of a correction for dust extinction. Other factors causing scatter include different SFHs, metallicities, as well as different population synthesis models and even IMFs (Gunawardhana et al. 2011). However, dust extinction dominates among these factors. Furthermore, the star-forming S_{HI} galaxies have on average bluer $(NUV - r)_0$ colors than the S_{opt} ones (median 1.42 versus 1.74 mag). Meanwhile, the tail of red and low SSFR galaxies in panel (a) disappears in panel (b), again reflecting the bias present in the HI-selected population. An additional result of the HI-selection is that the typical error bar in panel (b) is slightly smaller than in (a).

The lower panels in Figure 8 examine the optical SDSS colors $(u - r)_0$. As discussed previously in §2.2, on average $\delta(u - r)/\delta(NUV - r) \sim 0.6$. Figure 8(c) shows that galaxies with $SSFR \lesssim 10^{-11} \text{ yr}^{-1}$ have similar $(u - r)$ colors, forming a vertical tail in these plots; this red tail is much less pronounced in panel (d). The adoption of $(NUV - r)$ as the color index breaks down the degeneracy of $(u - r)$ in the red range ($u - r \gtrsim 2.3$) when inferences on the SFH are inferred. Furthermore, the SSFR correlates more linearly with $(NUV - r)_0$ than with $(u - r)_0$, e.g. $r_P = -0.95$ versus -0.87 in S_{opt} .

Given a simple assumption of the dust and stellar geometry, a well calibrated $IRX - \beta$ relation (IRX , infrared-excess defined as L_{TIR}/L_{FUV} ; β , the UV spectral slope) is sufficient to predict the A_{FUV} (tightly correlated with IRX) from the

UV color (characterizing the UV spectral slope, β), in starburst galaxies (Calzetti et al. 1994). However, the $IRX - \beta$ relation in normal star-forming galaxies has a shallower slope with larger scatter (Salim et al. 2007). This result may be due to differences in the SFH (Kong et al. 2004), or dust geometry (Cortese et al. 2006). Therefore, the loci of galaxies on an A_{FUV} versus $(FUV - NUV)$ plot give an indication of the dust extinction behavior.

Following this approach, the two samples S_{HI} and S_{opt} are compared in Figure 9, with results for S_{opt} on the left and S_{HI} on the right, both before and after applying the weight correction (see §4.1) in the upper and bottom rows respectively. The red dashed line corresponds to the fit to star-forming galaxies derived in Salim et al. (2007), based on a typical local SDSS-GALEX cross-matched catalog. Despite the large scatter, it is on average in close agreement with the distribution of the S_{opt} galaxies. Galaxies closer to the fit have overall higher weights so that the correlation appears to be slightly tighter in panel (c) than in (a). However, the distribution of the S_{HI} galaxies is offset from the fit in panels (b) and (d), toward the lower A_{FUV} side, i.e. for a given $(FUV - NUV)$ color, the HI-selected galaxies on average have lower extinctions. This result is also confirmed by the generally lower A_{FUV} of the S_{HI} sample overall, with a median value of 1.31 mag, relative to that of S_{opt} , 1.46 mag. Such a deviation of the main trend from the SF-fit of Salim et al. (2007) suggests that the HI-selected galaxies have different SFHs or dust geometries.

Unfortunately, the metallicity of the stellar population is poorly constrained by the SED-fitting. Nevertheless, given the correlation between dust and metallicity (e.g. Draine et al. 2007), the lower extinction infers that the S_{HI} galaxies have lower metallicity. Besides the well-known mass-metallicity (gas-phase) relation (e.g. Tremonti et al. 2004), Mannucci et al. (2010) demonstrate that at lower $M_* (< 10^{10.9} M_\odot)$, metallicity decreases sharply with increasing SFR, while at high stellar mass, metallicity does not depend on the SFR. Given the bias towards high SFR of the S_{HI} sample at a given M_* (see §4.2.4), the bias towards low metallicity and low extinction is expected. The gas-phase metallicity measures (oxygen abundance) from the MPA-JHU DR7 release (Tremonti et al. 2004) are available for 4211/7157 of the S_{HI} galaxies and 10311/16817 of the S_{opt} galaxies. In addition to the caveat of the small SDSS fiber aperture, the requirement of being an SDSS spectroscopic target may reduce the difference between the two subsets. The mean $12 + \log(O/H)$ is only slightly higher among the S_{opt} galaxies (8.74) than in the S_{HI} galaxies (8.71). The overall lower extinction among the S_{HI} galaxies is consistent with the idea that HI-selected galaxies are relatively gas rich and less evolved, with more likely gas infall, lower SFE and metallicity, less dust and thus lower extinction.

4.2.3. Distribution in the intrinsic CMD

The bimodal distribution in the optical CMD (Baldry et al. 2004) has been interpreted as an evolutionary sequence, with the blue-cloud galaxies growing through mergers and the consumption of gas and later migrating to the red sequence. This evolutionary scenario also predicts that galaxies evolve from a state of low stellar mass, high SSFR and high HI fraction to the opposite. As discussed in §3.1, the HI fraction is lower in redder galaxies leading to the result that an HI-selected sample like S_{HI} is biased against red galaxies whereas those are commonly included in, and may even dominate, an optically-selected one like S_{opt} . Here, we use the CMD to quantify this

bias.

Figure 10 shows the CMDs of the S_{opt} (left panels) and the S_{HI} (right panels); before and after applying weight corrections in the upper and bottom rows respectively. In these plots, absolute magnitudes $(M_r)_0$ and $(u-r)_0$ colors are corrected for internal extinction as given by the SED-fitting with the prior applied. A similar CMD for the whole $\alpha.40$ -SDSS population but without corrections can be found in Figure 7 of Haynes et al. (2011). The dash-dotted curve is based on the best fit to the division of the red and blue populations derived by Baldry et al. (2004) but with shifts toward bluer colors and brighter M_r applied in the amount of the mean extinction of the S_{opt} sample.

As is obvious in panels (a) and (b), the red sequence is far more pronounced in S_{opt} than in S_{HI} . Among the S_{opt} galaxies, only 68% lie on the blue side of the division, whereas the percentage of blue galaxies in the HI-selected S_{HI} population is as high as 84%. The small population of ‘red’ galaxies with HI represents candidate objects which (i) have recently migrated onto the red sequence retaining some residual gas, or (ii) will transit back to the blue cloud via late gas re-accretion (Cortese & Hughes 2009). Note that most of the red HI-bearing galaxies optically luminous. The HI mass of the faint red galaxies is usually so low that their HI line flux densities are below the sensitivity limit of ALFALFA.

In the V_{sur}/V_{max} weight corrected diagrams (panels c and d), the peaks of number density shift to fainter $(M_r)_0$ in both samples. Galaxies densely occupy the faintest $(M_r)_0$ bins, especially in the S_{opt} sample. This result is consistent with the optical luminosity function of the blue population (Baldry et al. 2004). A peak of the number density on the red sequence around $(M_r)_0 \sim -21$ also coincides with the maxima of the luminosity function derived by Baldry et al. (2004). However, a second peak appears on the red sequence at the faint end. Note that the data points in Baldry et al. (2004) also suggest a rise in number density in the faintest bins of the red sequence luminosity function (see their Figure 7), though those authors ignore these objects when they fit the Schechter function. In agreement with this, Hogg et al. (2003) reported a non-monotonic density trend along the red sequence, seen as a dip in the typical density for intermediate-mass red-sequence galaxies despite higher densities at higher and lower masses. Similar to the finding of a sudden broadening in the SSFR distribution faintwards of $M_B \sim -15$ (Lee et al. 2007), a sudden broadening in the color distribution faintwards of $(M_r)_0 \sim -16$ is seen in the S_{opt} sample. This increased spread suggests that, unlike the galaxies of intermediate mass in which the SF is mainly regulated by stellar mass and for which the blue population dominates in number, the gas in dwarfs can be easily removed so that SF suddenly quenches driving their migration onto the red sequence.

Figure 10(c) shows a CMD for an optically-selected population similar to Figure 2 of Baldry et al. (2004). However, S_{opt} is limited to $cz < 15000 \text{ km s}^{-1}$ whereas the low-redshift sample Baldry et al. (2004) studied has $1200 \text{ km s}^{-1} < cz < 24000 \text{ km s}^{-1}$. The imposition of the volume cut here clearly decreases the presence of luminous red galaxies; the local volume is dominated by blue star-forming galaxies. This effect is also enhanced by the additional UV selection applied to the S_{opt} sample.

The near-absence of the red sequence among the S_{HI} population is clear in panel (d); as we have noted before, a blind HI survey like ALFALFA is highly biased against red sequence galaxies. Additionally, in both populations galaxies appear

to be bluer as their M_r gets fainter, though with large scatter. Such a trend is weaker but still visible after internal extinction corrections are applied. Therefore, the slope is not only due to extinction, but is intrinsic.

Besides comparing the CMDs of S_{opt} and S_{HI} , we can also study the impact of HI selection through an examination of the fraction of S_{opt} galaxies that are cross matched to $\alpha.40$. As was discussed in §4.1, 34% of the S_{opt} galaxies are cross-matched to the $\alpha.40$ catalog. However, we note that such a fraction is a lower limit of the HI-detection rate of optical-UV selected galaxies in $\alpha.40$, because some S_{opt} objects may be a shredded photometric object of a gas bearer while another piece is cross-matched to the $\alpha.40$ entry. The fraction of these objects should however not be large (see Haynes et al. 2011).

Figure 11 explores the fraction of the S_{opt} population included in the $\alpha.40$ within the CMD (left) and the $SSFR-M_*$ diagram (right). In the left panel, the NUV-to-optical CMD with internal extinction corrections is color coded by the fraction of galaxies in the optically-selected S_{opt} sample which are also included in the $\alpha.40$; the contours trace the total number density of the S_{opt} galaxies. Clearly, an HI survey like ALFALFA is more efficient at detecting blue galaxies than red ones. Especially at very bright end of the blue cloud (lower left corner), the detection rate is close to 100%. Furthermore, the ALFALFA population also detects the majority of optically faint blue galaxies with the detection rate again approaching $\sim 100\%$ (lower right corner). The latter have the highest HI fractions (see also Figure 5). HI survey is most efficient in detecting galaxies with large diameter and high M_{HI}/L values (Garcia-Appadoo et al. 2009). The general shape of the color scale variation above a cross-match rate of $\sim 40\%$ resembles that of the number density variation on the blue side of the blue cloud. In contrast, starting from the red edge of the blue cloud and throughout the whole red sequence region, the rate of detection by ALFALFA drops below 10% and even to $\sim 0\%$. These results again demonstrate that HI-selection is highly biased against galaxies on the red sequence and furthermore, that such bias begins to become pronounced on the redder portions of what still is considered the blue cloud. The precise location of this limit to some extent reflects the ‘fast’ nature of ALFALFA (only 40 seconds integration per beam); a deeper survey of comparable solid angle would probe to lower gas fractions and hence deliver a higher cross-match rate.

4.2.4. Star-formation sequence

The scaling relation that the SFR increases with M_* among the $\alpha.40$ galaxies is demonstrated in §3.2 (Figure 4a). Figure 4(d) similarly shows the well confined star forming sequence in the $SSFR-M_*$ diagram. Based on the ES-SDSS sample, West et al. (2009) suggested that the significant offset towards bluer colors, induced by HI-selection can be explained by enhanced recent bursts of star formation. Furthermore, rising SFHs, i.e. high b -parameter, are required to explain the colors of HI-selected galaxies bluer than $g-r < 0.3$, which may result from gas infall and enhanced SF subsequently. Here, we compare the distributions of the S_{HI} and S_{opt} galaxies, on and off the star-forming sequences to explore further the impact of HI-selection.

Figure 12 examines the SFR versus M_* scaling relation for the optical (left) and HI (right) selected samples. The upper row shows the individual galaxies while the lower traces the V_{sur}/V_{max} weighted distributions. The cyan dashed line at $M_* \geq 10^{10} M_\odot$ shows the fit to this relation obtained by

Schiminovich et al. (2010), based on the high M_* GASS sample in all four panels:

$$\log\langle SFR(M_*) \rangle = 0.15 \log M_* - 1.5, \quad \log M_* > 10.0.$$

Like S_{opt} , GASS is essentially an SDSS selected sample but only includes the high stellar mass end. The blue diamonds and lines represent $\log\langle SFR \rangle$ derived for S_{opt} or S_{HI} in each stellar mass bin. Note these are different from the average trends in Figure 2 or Figure 4. The values are weighted averages in the weighted panels. The numbers of galaxies in each stellar mass bins are listed at the top of panels (a) and (b). Typical error bars are shown in panels (a, b).

The main distribution, consisting of the star forming galaxies, is associated with the parameter space inside the contours. In the un-weighted diagrams, the GASS fit is consistent with S_{opt} in the high mass range (panel a), but falls below the average of S_{HI} (panel b). This offset indicates that even when only the star forming sequence is considered, an HI-selected population has a higher SFR overall, because S_{HI} is not complete even within the blue population (see also Figure 11). Similarly, the blue diamonds in the weighted S_{opt} plot roughly coincide with the GASS fit (panel c). At the same time, the $\log\langle SFR \rangle$ of S_{HI} galaxies becomes systematically larger than the GASS fit with increasing M_* (panel d).

Below the locus of star forming galaxies, the S_{opt} sample contains a large population of passive galaxies visible as the cloud of points extending to very low SFRs (panel a). However, this population is barely seen in the same diagram for the S_{HI} galaxies (panel b), i.e. an HI-selected sample is highly biased against non-star-forming galaxies.

Because S_{opt} is truncated at the low mass end due to the applied V_{sur}/V_{max} weight limit (see §4.1), S_{HI} probes to lower M_* and thus lower SFRs on average. Despite this dwarf tail, the average SFR is still slightly higher in S_{HI} . The median SFR is $0.4 M_\odot \text{ yr}^{-1}$ in S_{opt} versus $0.6 M_\odot \text{ yr}^{-1}$ in S_{HI} . In the weighted plots, the correlation extending to the low M_* range is better illustrated (panel d). There is a hint of a change of slope in the $SFR-M_*$ scaling relation below the SF transition mass $M_* \simeq 10^{9.5} M_\odot$ noted earlier (§3.2 and equation 8), with the slope at high M_* being shallower, especially evident in the S_{opt} plots. We note that the trend appears to flatten again in the lowest M_* bin in panel (c) because of the weight cut. To be more specific, at a given M_r , the bluer galaxies with higher SSFRs have on average lower stellar masses, according to the mass-to-light ratio versus color relation. Therefore, the uniform M_r cutoff applied on the S_{opt} sample makes the distribution of M_* extend to lower limits in higher SSFR bins; this effect is visible in the S_{opt} diagrams (Figure 12a, c; see also the right panel of Figure 11). This effect artificially results in the higher $\log\langle SFR \rangle$ value in the lowest stellar mass bin. Furthermore, the lowest M_* bin only contains 70 galaxies, so that the average is even less reliable for statistical reasons. Such a sudden flattening is not seen within the S_{HI} population (panel d), which probes to lower M_* and with better sampling.

Figure 13 shows similar plots of the $SSFR - M_*$ correlation. The cyan dashed line again denotes the $\log\langle SSFR \rangle$ values tabulated in Schiminovich et al. (2010), derived from the high M_* GASS sample. The contoured region roughly represents the star forming sequence defined in Salim et al. (2007). The red dashed line is the fit of the sequence to the blue galaxies ($NUV - r < 4$) only as derived by those authors for a typical local SDSS-GALEX cross-matched catalog, with the

majority falling in the stellar mass range of $10^8 - 10^{10} M_\odot$:

$$\log SSFR = \begin{cases} -0.17(\log M_* - 10) - 9.65, & \log M_* \leq 9.4 \\ -0.53(\log M_* - 10) - 9.87, & \log M_* > 9.4. \end{cases}$$

For comparison, the blue diamonds in Figure 13 are derived for our datasets but also considering only the blue galaxies ($NUV - r < 4$). Note these fits are different from the one given as equation 8, shown in Figure 4(d).

Similar to what was seen in Figure 12, the S_{HI} population has on average higher SSFRs than the S_{opt} galaxies. The median SSFR is $10^{-9.95} \text{ yr}^{-1}$ for S_{opt} versus $10^{-9.72} \text{ yr}^{-1}$ for S_{HI} . The breakdown of the star forming sequence above stellar mass $\sim 2 \times 10^{10} M_\odot$ is only evident among the S_{opt} population, whereas comparably low SSFR galaxies are almost entirely absent from the S_{HI} sample. The GASS result agrees with the contours of S_{opt} above $10^{10} M_\odot$ (panel a and c), but lies below the average of S_{HI} (panel b and d).

In panel (c), the contours, associated with the high number density regions, that fall far below the main star forming sequence ($\log SSFR < -11$) mostly show up only at the highest and lowest M_* ends, suggesting that the scatter in the SSFR distribution is larger at both M_* ends than in intermediate mass range. However, the effective M_r cutoff applied to S_{opt} inhibits us from a more convincing conclusion on the possible breakdown of the star forming sequence at the low mass end.

At the high M_* end, the averaged SSFRs are systematically higher in the S_{HI} population than in the S_{opt} one. However, when only blue galaxies are considered in either sample, the discrepancy between the two is reduced so that the trends indicated by the blue diamonds are comparable in both. The blue diamonds are in good agreement with the definition of the star forming sequence in Salim et al. (2007), particularly for the high mass galaxies ($M_* \gtrsim 10^{9.4} M_\odot$) in the weighted plots, whereas the S_{HI} distribution is slightly offset to higher SSFRs in an un-weighted plot (panel b). In addition, note that we obtain a steeper slope than the blue fit in Salim et al. (2007) for low mass galaxies, even in the S_{opt} sample. Again because of the cutoff applied to S_{opt} , the averaged SSFR value in the lowest mass bin is artificially high.

Finally, we inspect the cross-match rate of S_{opt} to $\alpha.40$ over the $SSFR - M_*$ diagram in the right panel of Figure 11. The detection rate is the highest among galaxies with high SSFRs at both high and low M_* ends (above $\sim 60\%$) and is close to the overall average ($\sim 40\%$) throughout the high number density region along the star forming sequence. However, it drops to below $\sim 20\%$ from the lower edge of the star-forming sequence, and the slope of the low match rate division, which corresponds to a cross-match rate of $\sim 25\%$ (yellow band in this plot), coincides well with that of the star-forming sequence. The SF properties of a galaxy have a significant impact on its likelihood of detection by an HI survey.

We again note that the blue diamonds in Figure 13(b) are slightly above the red dot-dashed line suggesting that not all star-forming galaxies are detected by ALFALFA. From the fact that the HI detection rate of the galaxies in the SF sequence is far from 100% (see right panel of Figure 11), one may naively conclude that not all star-forming galaxies contain HI. However, this conclusion is not necessarily correct. For example, given the beam size of the ALFA frontend ($\sim 3.5'$), confusion can contribute to a lower effective detection rate, e.g. when a close pair of star-forming HI bearing galaxies is unresolved. In fact, the red dot-dashed line is in

excellent agreement with the blue diamonds in Figure 13(d), indicating that the mean trend of the star forming sequence can be well reproduced by the $\alpha.40$ galaxies *after* volume correction. An HI-selected sample can effectively trace the average of the star forming sequence despite the non-detection of some star-forming galaxies by ALFALFA (which is by design a short-integration time survey). In order to predict the SSFR of an HI-selected sample, one should still use equation (8) rather than the average scaling relations derived in this section. The latter relations, as well as the star forming sequence derived in Salim et al. (2007) rely on additional information, e.g., UV magnitudes or emission lines, to define the star-forming galaxies. However, the $(NUV - r) < 4$ (or similarly $\log SSFR < -11 \text{ yr}^{-1}$) is crude, since the SSFR generally decreases with increasing M_* . Furthermore, there are actually some very low SSFR galaxies detected in HI (e.g. Hallenbeck et al. 2012). Direct adoption of the SF sequence defined in Salim et al. (2007) will overpredict the SSFR of an HI-selected sample.

5. THE HOST HALOS OF HI-SELECTED GALAXIES

The results of the previous sections suggest that HI blind surveys detect in abundance the star-forming population but are highly biased against red sequence galaxies. Conversely, nearly all star-forming galaxies contain HI. Because ALFALFA is both wide area and sensitive, it samples the HI mass function over 4 orders of magnitude $7 < \log M_{HI} < 11$ with a mean of 9.56 dex (Martin et al. 2010) and, while not as deep as the SDSS, both surveys probe the same range of M_r . The brightest and reddest galaxies are missing from $\alpha.40$, but an HI-selected sample provides an important perspective on the star forming sequence. While galaxies in rich clusters are well known to be HI deficient because of the secular evolutionary processes (ram pressure stripping, thermal viscosity, harassment), HI-bearing galaxies dominate the extragalactic population in the low density field. As discussed in §3.2, the ALFALFA galaxies have, on average, lower SFEs, and equivalently therefore, longer t_R than the optically selected population. Both this work and the study of the lowest HI mass dwarf population by (Huang et al. 2012) suggest that overall, the HI-selected population is less evolved and has higher SFR and SSFR but lower SFE and extinction than one selected by optical brightness or stellar mass.

Perhaps the most surprising result of the ALFALFA survey has been the detection of a large number of galaxies with very high HI masses, $\log M_{HI} > 10.3$, including a significant number with abnormally high HI gas fractions (for their stellar mass), dubbed the HIgh HI Mass (HIghMass) galaxies. The existence of this population, albeit rare, begs the question: how can such massive disks retain their huge gas reservoirs *without* forming stars? One explanation is that, while recent inflow of HI gas has taken place, SF in that gas has not yet been triggered. Alternatively, the overall low SFEs characteristic of the ALFALFA population may be explained by the semi-analytic models of galaxy formation in Boissier & Prantzos (2000), which predict that more extended disks with larger scale length and lower stellar surface density are associated with dark matter halos of high spin parameter λ . Selected examples of very massive but gas-rich galaxies have been studied in recent years (e.g., Portas et al. 2010), with most belonging to the extreme category of low surface brightness (LSB) galaxies known as the “crouching giants” (Disney & Phillipps 1987) or “Malin 1 cousins” (Bothun et al. 1987; Impey & Bothun 1997). Their character-

istic huge size, low optical surface brightness, star formation rate and low metal abundances may be explained by the large angular momentum and thus the low surface density of their ISM; star formation in such disks is suppressed according to canonical star formation laws. However, we note that many of the HIghMass galaxies are not crouching giants. Instead of being quiescent objects like Malin 1, most of the HIghMass galaxies have blue disks and exhibit healthy on-going SF.”

The discussion throughout this paper is based on the scenario of hierarchical galaxy formation through mergers. Alternatively, cold mode accretion (Kereš et al. 2005) can build up gaseous galaxies rapidly at high redshift ($z > 1$). In the local universe volume probed by ALFALFA, it is likely that a large fraction of the gas accretion happens in a slower “hidden” mode, e.g., from the ionized hot corona or driven by the galactic-fountain process (Marinacci et al. 2010). In a future work, we will investigate the angular momentum distribution in the HIghMass galaxies to investigate whether the majority of the HI in local gas-rich galaxies reaches the assembling halo through filaments of cold flow at high redshift or results from gradual cooling out of the hot corona.

According to the Boissier & Prantzos (2000) model, for a given halo mass, galaxies whose halos are characterized by different values of λ have similar stellar masses and current SFRs. However, galaxies in high λ halos exhibit higher gas fractions, lower metallicities and bluer colors than those in low λ halos. In this picture, the halo mass controls current absolute values while the spin parameter determines mainly the shape of the SFH. Blue colors indicate high SSFRs, i.e., suppressed SF in the past relative to the current SFR. Massive compact disks have the shortest time scales of gas infall, rapid early SF, and thus are dominated by old stars today. In contrast, the low mass galaxies reside in high λ halos can even have a rising SFH instead of an exponentially decaying one; their timescales of gas infall, as well as SF, are long. This picture agrees with the downsizing scenario of galaxy formation (§3.2).

Meanwhile, the low stellar surface density found in gas-rich systems results in a weaker gravitational field, and, by extension, a lower mid plane gas pressure and a higher fraction of diffuse HI gas (Ostriker et al. 2010). The model constructed by Fu et al. (2010), tracking both the atomic and molecular gas in disk galaxies, predicts a low HI to H₂ conversion efficiency in the high λ galaxies. The HI, stellar and SF properties of the $\alpha.40$ -SDSS-GALEX galaxies, relative to the other local samples, therefore suggest that the HI-selected galaxies are biased towards ones in high λ halos, and thus are blue, inefficient in SF and less evolved. Nevertheless, they have comparable or even slightly higher current SFRs relative to the ones in the low λ halos with similar halo mass (see §4.2.4). In this section, we test this hypothesis.

5.1. Spin parameters derived from the Tully-Fisher relation

In their analysis, Boissier & Prantzos (2000) adopted the scaling properties derived by Mo et al. (1998), in the framework of the CDM scenario for galaxy formation. In this scenario, primordial density fluctuations give rise to dark matter halos of maximum rotational velocity V_{halo} , with the mass of the halo $M_{halo} \propto V_{halo}^3$. Inspired by theoretical studies to break the degeneracy, a second parameter, the spin parameter λ , is introduced to describe the halo (e.g. Mo et al. 1998), defined as $\lambda = J|E|^{1/2}G^{-1}M_{halo}^{-5/2}$, where J is the angular momentum and E is the total energy of the halo. Observationally,

λ is seen to determine properties such as color, disk thickness and bulge-to-disk ratio (Hernandez & Cervantes-Sodi 2006). Within the halo, baryonic gas condenses later and forms the stellar disk with mass M_* and characterized by an exponential surface density profile with disk scale length R_d . Those authors also assumed that the density profile of the dark matter halo is isothermal and responsible for establishing the flat disk rotation curve V_{rot} . Under the further assumptions that the potential energy of the galaxy is dominated by that of the halo and that it is a virialized gravitational structure, etc., Boissier & Prantzos (2000) related the quantities describing the halo to those describing the disk, and express the spin parameter as

$$\lambda = \frac{\sqrt{2}V_{rot}^2 R_d}{GM_{halo}}. \quad (9)$$

See also Hernandez & Cervantes-Sodi (2006) for similar derivation of equation (9). The only unobservable quantity M_{halo} can be replaced by M_{baryon}/F where F is the baryonic fraction, or, alternatively, M_*/F_d where F_d is the stellar disk mass fraction.

Based on this framework Hernandez et al. (2007) analyzed the empirical λ distribution of samples taken from the SDSS. Because their sample lacked direct measures of V_{rot} , those authors invoked the Tully-Fisher relation to infer V_{rot} from the disk luminosity. Furthermore, a disk mass Tully-Fisher relation and a constant disk mass fraction $F_d = 0.04$ are assumed to eliminate the M_{halo} term. As a first approach for direct comparison with Hernandez et al. (2007), we repeat the method used in that work to derive the distributions, separately, of the λ spin parameter for the HI-selected S_{HI} and the optically-selected S_{opt} galaxies. We adopt the λ estimator proposed by Hernandez et al. (2007),

$$\lambda = 21.8 \frac{R_d[\text{kpc}]}{(V_{rot}[\text{km s}^{-1}])^{3/2}}. \quad (10)$$

Hernandez et al. (2007) adopted the R -band Tully-Fisher relation derived by Barton et al. (2001) to assign V_{rot} to the observed galaxies; since this relation is valid only over the absolute magnitude range $-20 > M_R > -22.5$, they restrict their analysis to that range. To minimize errors due to internal extinction, they trim the sample to leave only spiral galaxies (Park & Choi 2005) having $b/a > 0.6$.

The R -band luminosity is inferred from the SDSS bands based on Lupton (2005),

$$(M_R)_0 = r_0 - 0.2936 \times (r - i)_0 - 0.1439.$$

We applied the same absolute magnitude cut $-20 > (M_R)_0 > -22.5$ to both the S_{HI} and the S_{opt} samples. Within our distance range, the SDSS is volume limited to $M_r \sim -19$ mag (Figure 6a). We also require that the r -band light profile should be better fitted by an exponential profile than a deVaucouleurs profile to be sure we were including mainly disk galaxies. Since Hernandez et al. (2007) ignored internal extinction but we have corrected for it using the SED fitting estimate of A_R , the b/a requirement in our case is less strict, $b/a > 0.35$. Such a cut is adopted so that the b/a distribution is close to being flat above 0.35. Like Hernandez et al. (2007), we convert the SDSS r -band axial ratio to inclination i ,

$$\cos^2 i = \frac{(b/a)^2 - q_0^2}{1 - q_0^2},$$

adopting an intrinsic axial ratio of the disk of $q_0 = 0.18$ as proposed by Courteau (1997). We note, however, that since that study was restricted to a relatively small number of Sb-Sc galaxies, a more conventional value of $q_0 = 0.2$ may be more appropriate (see §5.2).

First, we confirm that the TF relation Hernandez et al. (2007) used is systematically consistent with the S_{HI} galaxies, albeit with significant scatter. The HI line width of the S_{HI} galaxies, W_{50} , is converted to V_{rot} through $V_{rot} = (W_{50}/2/\sin i)$, where the small broadening effect (~ 5 km s $^{-1}$) of turbulence and non-circular motions on the observed HI linewidths is ignored. The average trend evident between $(M_R)_0$ and V_{rot} agrees with the relation, i.e., applying such a TF relation should have little effect on the mean value of the λ distribution. The difference of the mean λ value derived here as compared with that derived next in §5.2 will be mainly due to the different assumptions of the baryon fraction F .

Next, we obtain the λ distributions of the S_{HI} and the S_{opt} samples, according to equation (10), and following Hernandez et al. (2007), we confirm that they both are well fit by a lognormal function:

$$P(\lambda_0, \sigma_\lambda; \lambda)d\lambda = \frac{1}{\sigma_\lambda \sqrt{2\pi}} \exp\left[-\frac{\ln^2(\lambda/\lambda_0)}{2\sigma_\lambda^2}\right] \frac{d\lambda}{\lambda}.$$

The best fit parameters are $\lambda_0 = 0.0525$, $\sigma_\lambda = 0.422$ for the S_{HI} distribution of the HI selected galaxies S_{HI} and $\lambda_0 = 0.0489$, $\sigma_\lambda = 0.446$ for the SDSS-selected S_{opt} distribution. Because we correct M_R for extinction, our λ_0 value is slightly below the value found by Hernandez et al. (2007), $\lambda_0 = 0.0585$. While suggestive, this difference of λ_0 between the two samples S_{HI} and S_{opt} , under the assumption of a constant disk-to-total mass fraction F_d , is small. The various cuts and selection effects applied to both samples, e.g. detected in UV, better fit by an exponential profile, small dynamic range of M_r , may have already minimized the possible difference in λ_0 within the full sample. Given that the remaining galaxies in the S_{HI} sample are brighter on average than those in the S_{opt} sample, i.e., V_{rot} is higher on average, the slightly higher λ_0 found by this analysis is due to the fact that S_{HI} galaxies have on average larger R_d values (see equation 10). HI selection instills a bias towards more extended galaxies.

5.2. λ distribution of the parent population

The SDSS galaxies analyzed by Hernandez et al. (2007) lack direct measurements of V_{rot} , whereas the $\alpha.40$ -SDSS-GALEX sample has homogeneous W_{50} measurements for all its galaxies. We hence improve the derivation of the λ distribution for all the $\alpha.40$ -SDSS-GALEX galaxies in this section. Assuming that an HI-selected sample has little contamination from galaxies which are not disk dominated, we drop the requirement of a higher probability of an exponential fit and adopt an intrinsic $q_0 = 0.2$. Because HI line widths are available, we no longer rely on the Tully-Fisher relation to infer V_{rot} , and for that reason, the $(M_r)_0$ limit is also dropped. Most importantly, we estimate λ directly from equation (9) assuming a non-constant F to derive M_{halo} .

Following Hernandez et al. (2007), the preceding assumes that all halos are associated with the same disk mass fraction $F_d = 0.04$. However, based on abundance matching between the observed stellar mass function and dark matter halo mass function derived from CDM simulations, it is quite well established that F_d is not a constant (Behroozi et al.

2010, and references therein). Instead, the distribution of F_d as a function of M_{halo} peaks around $M_{halo} \sim 10^{12} M_\odot$ (e.g. Guo et al. 2010), i.e., low mass galaxies, corresponding to $M_* \lesssim 10^{10.5} M_\odot$, retain fewer baryons as their halo mass declines. The trend turns over above $M_* \sim 10^{10.5} M_\odot$. Based on the $\alpha.40$ catalog, Papastergis et al. (2011) have studied how galaxies with different V_{rot} populate dark matter halos, by applying similar abundance matching to the velocity width function, under the assumption that rotational velocity well traces the dark matter mass. We adopt the V_{halo} - V_{rot} relation from Table 1 of Papastergis et al. (2011), assuming $V_{halo,max} = 360 \text{ km s}^{-1}$. The resulting V_{halo} is converted into the virial mass of the halo following the simulation result of Klypin et al. (2011): $V_{halo} = 2.8 \times 10^{-2} (M_{halo} h)^{0.316}$. For the disk scale length R_d , we use that measured by the SDSS pipeline in the r -band,

Among the 9417 $\alpha.40$ -SDSS-GALEX galaxies, 1829 are dropped because of the adopted axial ratio cut ($b/a > 0.35$ as in §5.1), and a further 130 are dropped because they lie outside of the valid range of the V_{rot} - V_{halo} relation ($16 \text{ km s}^{-1} < V_{rot} < 431 \text{ km s}^{-1}$). In the end, λ values are estimated for 7458 $\alpha.40$ galaxies; their distribution is shown in the Figure 14(a). The black solid line traces the normalized PDF for the $\alpha.40$ galaxies. The red dash-dotted line in Figure 14(a) shows the best log-normal fit with $\lambda_0 = 0.0585$ and $\sigma_\lambda = 0.446$ from Hernandez et al. (2007) and the blue dashed line is the best fit to the $\alpha.40$ galaxies with $\lambda_0 = 0.0929$ and $\sigma_\lambda = 0.875$. Hernandez et al. (2007) noted that values they found for both λ_0 and σ_λ are in good agreement with results from cosmological simulations. However, the λ distribution of the $\alpha.40$ -SDSS-GALEX galaxies has a mean well above this value, $\lambda = 0.0852$. Furthermore, the distribution for the $\alpha.40$ -SDSS-GALEX sample has a much wider dispersion than the previous result, arising mainly from the fact that we adopt different F values according to the V_{rot} , rather than treating it as a constant. As a result, the distribution of spin parameters of the HI-selected population is no longer well fit by a lognormal function. The KS statistic implies that the probability that the λ distribution for the HI-selected population is drawn from the same underlying distribution with a PDF of the best-fit lognormal function with $\lambda_0 \sim 0.0929$ is negligible.

The technique of assigning M_{halo} is valid only in a statistical sense, rather than as a concrete measure for individual galaxies. For this reason, we look only for a general trend in the dependence of the luminous component on the λ of the halos. Figure 14(b) shows a f_{HI} - M_* diagram similar to Figure 2(c), but color coded by the mean λ value of galaxies in each grid. The black contours outline the distribution of the 7458 $\alpha.40$ galaxies in the high number density region. A trend is evident that, in a given M_* bin, the gas rich galaxies with higher f_{HI} on average reside in halos with higher λ . Meanwhile, along lines of constant M_{HI} (straight lines with slope of -1 in the f_{HI} - M_* diagram), $\langle \lambda \rangle$ barely changes with increasing M_* . Taking into account the mean scaling relation defined by the $\alpha.40$ galaxies (blue diamonds in Figure 2c) relative to the similar relations obtained for other samples, this result reinforces the hypothesis that the HI-selected galaxies favor high λ halos. The f_{HI} - M_* relations confined by the ‘HI-normal’ or the ‘outside Virgo’ galaxies in Figure 2(c) are close to the well accepted $\lambda \sim 0.05$ region, the yellow band in Figure 14(b).

We note that such a clear trend is only weakly due to the overall larger R_d , i.e., lower surface brightness, which the

more gas-rich galaxies have in a given M_* bin, but is instead largely due to the rapidly increasing $F = (M_{HI} + M_*)/M_{halo}$ with M_{HI} in a given M_* bin. However, it is known that the increase in F with M_{halo} is reversed near $M_* \sim 10^{10.5} M_\odot$. In fact, the variation of $\langle \lambda \rangle$ along the f_{HI} axis disappears around $M_* \sim 10^{10.5} M_\odot$ in Figure 14(b). In addition, we note that within the luminosity range of $-20 > (M_R)_0 > -22.5$, the stellar disk fraction, F_d , inferred by this method spreads over a range with a median of 0.04; the M_{halo} - F relation crosses the turnover around $(M_R)_0 \sim -21.5$. Despite the systematic variation of F_d we adopt, the median is consistent with the assumption followed in §5.1

Because the V_{rot} - V_{halo} relation we have used is less constrained at the highest masses, it barely reproduces the trend of decreasing F with M_{halo} above $M_* \sim 10^{10.5} M_\odot$. Alternatively, we can estimate the M_{halo} following the M_* - M_{halo} relation (Guo et al. 2010),

$$\frac{M_*}{M_{halo}} = 0.129 \left[\left(\frac{M_{halo}}{10^{11.4} M_\odot} \right)^{-0.926} + \left(\frac{M_{halo}}{10^{11.4} M_\odot} \right)^{0.261} \right]^{-2.440}$$

The fit is valid in the M_{halo} range of $10^{10.8}$ to $10^{14.9} M_\odot$, and thus describes better the most massive $\alpha.40$ galaxies. However, it cannot constrain the low mass HI-bearing halos. As expected, such a M_* - M_{halo} relation, with a turnover $M_{halo} \sim 10^{12} M_\odot$, produces a similar trend of the $\langle \lambda \rangle$ variation as seen in Figure 14(b) for galaxies with $M_* \lesssim 10^{10.5} M_\odot$. However, for the most massive galaxies with $M_* \gtrsim 10^{10.5} M_\odot$, such a trend disappears, and galaxies with similar M_* have similar λ , regardless of their f_{HI} . Meanwhile, $\langle \lambda \rangle$ turns over to decrease with increasing M_* with approximately constant M_{HI} .

As a result, the pattern of colors in Figure 14(b) predicts that the most gas rich ones with M_* near $10^{10} M_\odot$ should be associated with halos with the highest λ parameters. We are testing this prediction by studying the stellar, gas and dark matter components of a sample of very high HI mass ($M_{HI} > 10^{10} M_\odot$), high gas fraction (for their stellar mass) galaxies, the HighMass sample. Visual inspection of the HighMass galaxies shows that the ones with intermediate M_* shows the strongest color gradient (bluer in outer regions), as predicted for high λ galaxies (Hernandez & Cervantes-Sodi 2006). Future work will constrain the spin parameters using velocity fields derived from HI synthesis maps for 20 of the HighMass galaxies. Furthermore, the HI distributions and sites of star formation will be examined to yield more detail on the SFL and possible mechanisms which inhibit the formation of stars in these massive HI disks.

The HI, stellar and SF properties of the ALFALFA population as exemplified by the $\alpha.40$ -SDSS-GALEX galaxies suggest that the HI-selected population is biased towards extended disks which reside in high λ dark matter halos. As such, their disks are currently forming stars but in an inefficient manner. Despite the low SFE, such galaxies can have comparable or even slightly higher current SFRs relative to the ones in the low λ halos of similar halo mass (see §4.2.4). This combination of on-going star formation and inefficiency in the conversion of gas into stars causes their disks to be extended, blue and of low metallicity, suggestive of their being less evolved. Remembering too that the $\alpha.40$ galaxies are among the least clustered population (Martin et al. 2012), we are reminded that these systems likely follow a quite different, quiescent evolutionary history relative to galaxies residing in

higher density volumes. Although the details of the involved processes still elude us, the study of the ALFALFA population strongly suggests that where a galaxy is born and resides determines to a large extent how and when it converts its gas into stars.

6. CONCLUSION

Given the importance of proposed future extragalactic HI surveys at high redshift by the SKA, it is critical to develop a full understanding of the characteristics of gas rich galaxies at the present epoch. ALFALFA is an on-going blind HI survey, for the first time providing a full census of HI-bearing objects over a cosmologically significant volume of the local universe. Building on the $\alpha.40$ catalog (Haynes et al. 2011), we use the corresponding photometry available from the SDSS DR7 and GALEX GR6 catalogs to explore the population of galaxies detected by ALFALFA. The combined $\alpha.40$ -SDSS-GALEX sample includes 9417 galaxies. SED-fitting to the seven UV and optical bands yields the stellar properties of the HI-selected galaxies, including their stellar masses, SFRs and internal extinctions. The lack of a correction for internal extinction can lead to systematic underestimates of the optical luminosities and SFRs. In order to reduce the overestimate of internal extinction and thus the SFR with decreasing M_* while still accounting for the effect of dust in these mostly disk-dominated systems, we apply a prior distribution of τ_V in the fitting process. Although extinction is even more of an issue at the short wavelengths, the addition of photometry in the UV bands is critical to the diagnostic power of the SFH because the UV measures break the degeneracy evident in optical-only colors, particularly among the red sequence galaxies.

ALFALFA offers a complete statistical sampling of the full range of M_{HI} and M_* , from the most massive giant spirals with $M_{HI} > 10^{10} M_\odot$ to the lowest HI mass dwarfs with $\log M_{HI} < 10^{7.5} M_\odot$, thereby providing a firmer basis for the derivation of the fundamental scaling relations linking the global properties. First, we confirm the existence of the relations which have been found in typical local optical-UV catalogs (e.g. Salim et al. 2007). For example, (1) SFRs increase but SSFRs decrease with increasing M_* , with different slopes in the high and low M_* ranges, with the transition occurring at $M_* \sim 10^{9.5} M_\odot$; (2) the SSFR is tightly correlated with the $(NUV - r)$ color, especially after the latter is corrected for internal extinction. Second, we investigate similar relations involving the HI mass. For example, (3) SFRs also increase but SSFRs decrease with increasing M_{HI} , though with larger scatter. The HI gas contributes a significant fraction of the baryons in HI-selected galaxies, and their SFRs show a good correlation with M_{HI} , suggesting that a global, atomic, volumetric SFL applies in HI-selected systems. (4) The HI fraction, $f_{HI} \equiv M_{HI}/M_*$, nicely correlates with M_* , but a change in the slopes of the relation is evident near $M_* \sim 10^9 M_\odot$. (5) Galaxies with bluer colors in general have higher f_{HI} . (6) The star formation efficiency, $SFE \equiv SFR/M_{HI}$, mildly increases with stellar mass with a slightly steeper relation for $M_* \lesssim 10^{9.5} M_\odot$. In §3.1, we give the best linear fits to the principal scaling relations among the ALFALFA population, including the $M_{HI}-M_*$ and $SSFR-M_*$ correlations, as well as the fundamental planes of $f_{HI}-(NUV - r)-\mu_*$, etc. In particular, we argue that Equation (2-7) provides the most robust predictor based on optical properties of the detection rate by future HI line surveys with the SKA and its pathfinders.

Besides the scaling relations themselves, the combined $\alpha.40$ -SDSS-GALEX dataset, as a large and homogeneous sample with HI measures, enables the quantitative appraisal of the scatter in relations and a deeper understanding of the role HI plays in the galaxy evolution. In particular, the decreasing f_{HI} with increasing M_* is related to the star-forming sequence identified in the $SSFR-M_*$ diagram, or the evolutionary tracks of galaxies on the CMD, i.e. as galaxies assemble their stellar masses, they evolve gradually to relatively red and gas poor regimes, and also show lower SSFRs. Furthermore, *only* evident among the low mass galaxies ($M_* \lesssim 10^{9.5} M_\odot$), the galaxies with higher f_{HI} on average also have higher $SSFR$ in a given M_* bin. Similarly, within a given M_r bin, higher f_{HI} on average indicates bluer $(NUV - r)$ color. However, the corresponding trend that the HI-rich galaxies are more likely to be blue starburst galaxies with high SSFRs is weak among the high mass galaxies, i.e., the regulation of SF by HI is weaker in more massive systems. Similarly, the dispersion of the color distribution in a given M_r bin and the dispersion of the $SSFR$ distribution in a given M_* bin are both at a minimum near $M_* \sim 10^{9.5} M_\odot$, and both increase at masses lower than that. It appears that SF is no longer regulated principally by the stellar mass in low mass systems. In their shallow potential wells, gas can be easily removed so that the SF quenches causing the galaxy to migrate onto the red sequence.

We also focus on the nature of the population detected by the ALFALFA survey, in the context of populations better understood through observations at other wavelengths, e.g. optical or UV. The $\alpha.40$ galaxies on average have higher HI fractions in a given stellar mass bin, compared to the optically-selected samples, with an overall average of $f_{HI} \sim 1.5$. 95.6% of the $\alpha.40$ -SDSS-GALEX galaxies have $(NUV - r) < 4$ and belong to the blue cloud on a UV-to-optical CMD. The red ALFALFA detections include early type galaxies with quenched SF but unusually high HI masses, suggesting a recent acquisition of HI. The very blue HI-rich galaxies may be attributed to a SFH that steadily rises to the present day with little integrated past SF. The SFEs of the HI-selected galaxies are lower on average, or equivalently, their gas depletion timescales are longer (average $t_R = 8.9$ Gyr), compared to the high stellar mass galaxies included in the GASS survey (Schiminovich et al. 2010). Given the fact that the overall SFRs of $\alpha.40$ galaxies are even higher than those in GASS at a given M_* , the low SFEs found for HI-selected galaxies are caused by their high HI masses rather than by lower SFRs. This result is consistent with the idea that HI-selected sample is biased towards the most gas-rich galaxies and that the SFE is low in HI-dominated systems. A bottleneck may exist in the HI to H₂ conversion, or the process of SF from H₂ may obey an unusual SFL with low efficiency in the very HI-dominated galaxies. For a given $(FUV - NUV)$ color, HI-selected galaxies have on average lower extinctions, suggesting that they have different SFHs or dust geometries.

To quantify better the bias of the HI-selected population relative to the optically-selected galaxies, we constructed two volume-corrected control samples, starting from the $\alpha.40$ and the SDSS DR7 catalogs, which we designate S_{HI} and S_{opt} respectively. The HI-selected S_{HI} sample is found to be biased against red-sequence galaxies as well as massive but low SFR, low SSFR galaxies. However, if only the blue cloud galaxies with $(NUV - r) < 4$ are considered, both samples define similar SF sequences, i.e., an HI survey well samples the star forming population. For the SDSS-selected volume-limited

S_{opt} sample, the rate of detection by ALFALFA decreases towards redder colors. Virtually all very blue S_{opt} galaxies at both the high and low stellar mass ends are detected by ALFALFA; however, among the blue population, the HI detection rate drops to $\sim 40\%$ throughout the high number density region along the SF sequence. At the same time, only a very few of the galaxies which lie below the SF sequence in an $SSFR$ vs. M_* diagram are detected by ALFALFA. Furthermore, ALFALFA misses a substantial fraction of the optical galaxies lying on the redder side of the blue cloud. The volume-corrected optically-selected S_{opt} sample well reproduces various scaling relations derived from the high stellar mass GASS sample (Catinella et al. 2010; Schiminovich et al. 2010). However, at the highest stellar masses, the HI-selected S_{HI} galaxies show systematically larger discrepancies in their SF properties from the GASS results as the fraction of the total population which is detected by ALFALFA in a given stellar mass bin declines. In comparison with optically-selected samples, HI-selected galaxies that have high gas fractions are relatively less evolved and have, on average, bluer colors, higher SFRs and SSFRs, but lower SFEs, extinctions and metallicities.

Previous authors, notably Boissier & Prantzos (2000), have proposed that the overall low SFEs found in gas-rich systems may be explained if, their disks are characterized by large disk scale lengths and lower stellar surface densities because their host dark matter haloes have high spin parameters λ . We explore this hypothesis comparing the spin parameter distributions of the volume-limited S_{HI} and S_{opt} samples following the approach outlined in Hernandez et al. (2007) which estimates the V_{rot} using the Tully-Fisher relation. As presented by Hernandez et al. (2007), this estimate of λ assumes that all galaxies are characterized by the same disk mass fraction $F_d = 0.04$. Under that (unlikely) assumption, we find a spin parameter distribution close to that found by Hernandez et al. (2007) for their SDSS disk subsample and well-fit by a log normal distribution in agreement with numerical simulations. There is a slight hint that the HI-selected population S_{HI} has a slightly higher λ_0 than the S_{opt} sample which could reflect the bias that the HI-selected sample is characterized by more extended disks. However, abundance matching between the observed stellar mass functions and the CDM halo mass functions derived from simulations strongly suggests that that F is not a constant but rather peaks around a halo mass of $M_{halo} \sim 10^{12} M_\odot$ (e.g. Guo et al. 2010). At the low mass end, baryon depletion again grows in the shallow potential wells (Hoefl et al. 2006). Because the $\alpha.40$ catalog contains HI line widths, we calculate spin parameters from them adopting the $V_{halo}-V_{rot}$ relation from Table 1 of Papastergis et al. (2011). While this method of assigning M_{halo} is only valid in a statistical sense, the result is clear: the distribution of λ is no longer log normal and has a mean value well in excess of the expectation, strongly reinforcing the hypothesis that the ALFALFA population favors high λ dark matter hosts.

In the future, our multiwavelength program to study the HighMass sample of high gas fraction, high HI mass galaxies will explore the star formation process and the interrelationships of the stellar, gas, dust and dark matter components within this set of exceptionally massive HI disks. The Survey of HI in Extremely Low mass Dwarfs (SHIELD) is exploring similar relationships among the lowest HI mass galaxies detected by ALFALFA (Cannon et al. 2011) and has already uncovered evidence that the SFL in those galaxies is unusual.

The authors acknowledge the work of the entire ALFALFA collaboration team in observing, flagging, and extracting the catalog of galaxies used in this work. The ALFALFA team at Cornell is supported by NSF grants AST-0607007 and AST-1107390 to RG and MPH and by grants from the Brinson Foundation. We thank Manolis Papastergis for useful discussions.

The Arecibo Observatory is operated by SRI International under a cooperative agreement with the National Science Foundation (AST-1100968), and in alliance with Ana G. Méndez-Universidad Metropolitana, and the Universities Space Research Association.

GALEX is a NASA Small Explorer, launched in 2003 April. We gratefully acknowledge NASA's support for construction, operation and science analysis for the GALEX mission, developed in cooperation with the Centre National d'Etudes Spatiales of France and the Korean Ministry of Science and Technology. SH, RG and MPH acknowledge support for this work from the GALEX Guest Investigator program under NASA grants NNX07AJ12G, NNX07AJ41G, NNX08AL67G, NNX09AF79G and NNX10AI03G.

Funding for the SDSS and SDSS-II has been provided by the Alfred P. Sloan Foundation, the participating institutions, the National Science Foundation, the US Department of Energy, the NASA, the Japanese Monbukagakusho, the Max Planck Society and the Higher Education Funding Council for England. The SDSS Web Site is <http://www.sdss.org/>. The SDSS is managed by the Astrophysical Research Consortium for the participating institutions. The participating institutions are the American Museum of Natural History, Astrophysical Institute Potsdam, University of Basel, University of Cambridge, Case Western Reserve University, University of Chicago, Drexel University, Fermilab, the Institute for Advanced Study, the Japan Participation Group, Johns Hopkins University, the Joint Institute for Nuclear Astrophysics, the Kavli Institute for Particle Astrophysics and Cosmology, the Korean Scientist Group, the Chinese Academy of Sciences (LAMOST), Los Alamos National Laboratory, the Max Planck Institute for Astronomy, the MPA, New Mexico State University, Ohio State University, University of Pittsburgh, University of Portsmouth, Princeton University, the United States Naval Observatory and the University of Washington.

REFERENCES

- Abazajian, K. N., Adelman-McCarthy, J. K., Agüeros, M. A., et al. 2009, *ApJS*, 182, 543
- Abdalla, F. B., & Rawlings, S. 2005, *MNRAS*, 360, 27
- Baldry, I. K., Glazebrook, K., Brinkmann, J., et al. 2004, *ApJ*, 600, 681
- Barnes, D. G., Staveley-Smith, L., de Blok, W. J. G., et al. 2001, *MNRAS*, 322, 486
- Barton, E. J., Geller, M. J., Bromley, B. C., van Zee, L., & Kenyon, S. J. 2001, *AJ*, 121, 625
- Behroozi, P. S., Conroy, C., & Wechsler, R. H. 2010, *ApJ*, 717, 379
- Bell, E. F., McIntosh, D. H., Katz, N., & Weinberg, M. D. 2003, *ApJS*, 149, 289
- Bigiel, F., Leroy, A., Walter, F., et al. 2008, *AJ*, 136, 2846
- Bigiel, F., Leroy, A., Walter, F., et al. 2010, *AJ*, 140, 1194
- Bigiel, F., Leroy, A., Seibert, M., et al. 2010, *ApJ*, 720, L31
- Bigiel, F., Leroy, A. K., Walter, F., et al. 2011, *ApJ*, 730, L13
- Blanton, M. R., & Roweis, S. 2007, *AJ*, 133, 734
- Blanton, M. R., & Moustakas, J. 2009, *ARA&A*, 47, 159
- Blanton, M.R., Kazin, E., Muna, D., Weaver, B.A., & Price-Whelan, A. 2011, *AJ*, 142, 31
- Boissier, S., & Prantzos, N. 2000, *MNRAS*, 312, 398
- Boselli, A., Gavazzi, G., Donas, J., & Scodreggio, M. 2001, *AJ*, 121, 753
- Bothun, G. D., Impey, C. D., Malin, D. F., & Mould, J. R. 1987, *AJ*, 94, 23
- Bothwell, M. S., Kennicutt, R. C., & Lee, J. C. 2009, *MNRAS*, 400, 154
- Brinchmann, J., Charlot, S., White, S. D. M., et al. 2004, *MNRAS*, 351, 1151
- Calzetti, D., Kinney, A. L., & Storchi-Bergmann, T. 1994, *ApJ*, 429, 582
- Cannon, J. M., Giovanelli, R., Haynes, M. P., et al. 2011, *ApJ*, 739, L22
- Cardelli, J. A., Clayton, G. C., & Mathis, J. S. 1989, *ApJ*, 345, 245
- Catinella, B., Haynes, M. P., Giovanelli, R., Gardner, J. P., & Connolly, A. J. 2008, *ApJ*, 685, L13
- Catinella, B., Schiminovich, D., Kauffmann, G., et al. 2010, *MNRAS*, 403, 683
- Chabrier, G. 2003, *PASP*, 115, 763
- Cortese, L., Boselli, A., Buat, V., et al. 2006, *ApJ*, 637, 242
- Cortese, L., & Hughes, T. M. 2009, *MNRAS*, 400, 1225
- Cortese, L., Catinella, B., Boissier, S., Boselli, A., & Heinis, S. 2011, *arXiv:1103.5889*
- Courteau, S. 1997, *AJ*, 114, 2402
- Cowie, L. L., Songaila, A., Hu, E. M., & Cohen, J. G. 1996, *AJ*, 112, 839
- Charlot, S., & Fall, S. M. 2000, *ApJ*, 539, 718
- Davies, R. D., & Lewis, B. M. 1973, *MNRAS*, 165, 231
- Disney, M., & Phillips, S. 1987, *Nature*, 329, 203
- Disney, M. J., Romano, J. D., Garcia-Appadoo, D. A., et al. 2008, *Nature*, 455, 1082
- Donovan, J.L., Serra, P., van Gorkom, J.H., et al. 2009, *ApJ*, 137, 5037
- Draine, B. T., Dale, D. A., Bendo, G., et al. 2007, *ApJ*, 663, 866
- Fabello, S., Catinella, B., Giovanelli, R., et al. 2011, *MNRAS*, 411, 993
- Fu, J., Guo, Q., Kauffmann, G., & Krumholz, M. R. 2010, *MNRAS*, 409, 515
- Gallazzi, A., Charlot, S., Brinchmann, J., White, S. D. M., & Tremonti, C. A. 2005, *MNRAS*, 362, 41
- Garcia-Appadoo, D. A., West, A. A., Dalcanton, J. J., Cortese, L., & Disney, M. J. 2009, *MNRAS*, 394, 340
- Gavazzi, G., Pierini, D., & Boselli, A. 1996, *A&A*, 312, 397
- Gavazzi, G., Fumagalli, M., Galardo, V., et al. 2012, in preparation
- Gavazzi, G., Fumagalli, M., Galardo, V., et al. 2012, in preparation
- Giovanelli, R., & Haynes, M. P. 1985, *ApJ*, 292, 404
- Giovanelli, R., Haynes, M. P., Salzer, J. J., et al. 1995, *AJ*, 110, 1059
- Giovanelli, R., Haynes, M. P., Herter, T., et al. 1997, *AJ*, 113, 22
- Giovanelli, R., Haynes, M. P., Kent, B. R., et al. 2005a, *AJ*, 130, 2598
- Giovanelli, R., Haynes, M. P., Kent, B. R., et al. 2005b, *AJ*, 130, 2613
- Giovanelli, R., Haynes, M. P., Kent, B. R., et al. 2007, *AJ*, 133, 2569
- Giovanelli, R., Haynes, M. P., Kent, B. R., & Adams, E. A. K. 2010, *ApJ*, 708, L22
- Gunawardhana, M. L. P., Hopkins, A. M., Sharp, R. G., et al. 2011, *MNRAS*, 415, 1647
- Guo, Q., White, S., Li, C., & Boylan-Kolchin, M. 2010, *MNRAS*, 404, 1111
- Hallenbeck, G., Papastergis, E., Huang, S., et al. 2012, submitted
- Haynes, M. P., Giovanelli, R., Martin, A. M., et al. 2011, *AJ*, 142, 170
- Hernandez, X., & Cervantes-Sodi, B. 2006, *MNRAS*, 368, 351
- Hernandez, X., Park, C., Cervantes-Sodi, B., & Choi, Y.-Y. 2007, *MNRAS*, 375, 163
- Hoefl, M., Yepes, G., Gottlöber, S., & Springel, V. 2006, *MNRAS*, 371, 401
- Hogg, D. W., Blanton, M. R., Eisenstein, D. J., et al. 2003, *ApJ*, 585, L5
- Huang, S., Haynes, M. P., Giovanelli, R., et al. 2012, *AJ*, 143, 133
- Impey, C., & Bothun, G. 1997, *ARA&A*, 35, 267
- Kannappan, S. J. 2004, *ApJ*, 611, L89
- Kannappan, S. J., Guie, J. M., & Baker, A. J. 2009, *AJ*, 138, 579
- Kauffmann, G., Heckman, T. M., White, S. D. M., et al. 2003, *MNRAS*, 341, 33
- Kennicutt, R. C., Jr. 1998, *ApJ*, 498, 541
- Kereš, D., Katz, N., Weinberg, D. H., & Davé, R. 2005, *MNRAS*, 363, 2
- Klypin, A. A., Trujillo-Gomez, S., & Primack, J. 2011, *ApJ*, 740, 102
- Kong, X., Charlot, S., Brinchmann, J., & Fall, S. M. 2004, *MNRAS*, 349, 769
- Krumholz, M. R., McKee, C. F., & Tumlinson, J. 2008, *ApJ*, 689, 865
- Krumholz, M. R., McKee, C. F., & Tumlinson, J. 2009, *ApJ*, 693, 216
- Krumholz, M. R., McKee, C. F., & Tumlinson, J. 2009, *ApJ*, 699, 850
- Krumholz, M. R., Dekel, A., & McKee, C. F. 2011, *arXiv:1109.4150*
- Krumholz, M. R., Leroy, A. K., & McKee, C. F. 2011, *ApJ*, 731, 25
- Lee, J. C., Kennicutt, R. C., Funes, S. J., José G., Sakai, S., & Akiyama, S. 2007, *ApJ*, 671, L113
- Leroy, A. K., Walter, F., Bigiel, F., et al. 2009, *AJ*, 137, 4670
- Mannucci, F., Cresci, G., Maiolino, R., Marconi, A., & Gnerucci, A. 2010, *MNRAS*, 408, 2115
- Marinacci, F., Binney, J., Fraternali, F., et al. 2010, *MNRAS*, 404, 1464
- Martin, A. M., Papastergis, E., Giovanelli, R., et al. 2010, *ApJ*, 723, 1359
- Martin, A. M., Giovanelli, R., Haynes, M. P., & Guzzo, L. 2012, *ApJ*, 750, 38
- Masters, K. L., Mosleh, M., Romer, A. K., et al. 2010, *MNRAS*, 405, 783
- Meyer, M. J., Zwaan, M. A., Webster, R. L., et al. 2004, *MNRAS*, 350, 1195
- Mo, H. J., Mao, S., & White, S. D. M. 1998, *MNRAS*, 295, 319
- Moran, S. M., Kauffmann, G., Heckman, T. M., et al. 2010, *ApJ*, 720, 1126
- Morganti, R., de Zeeuw, P. T., Oosterloo, T. A., et al. 2006, *MNRAS*, 371, 157
- Morrissey, P., Conrow, T., Barlow, T. A., et al. 2007, *ApJS*, 173, 682
- Obreschkow, D., Klöckner, H.-R., Heywood, I., Levrier, F., & Rawlings, S. 2009, *ApJ*, 703, 1890
- Oosterloo, T. A., Morganti, R., Crocker, A. et al. 2010, *MNRAS*, 409, 500
- Ostriker, E. C., McKee, C. F., & Leroy, A. K. 2010, *ApJ*, 721, 975
- Papastergis, E., Martin, A. M., Giovanelli, R., & Haynes, M. P. 2011, *ApJ*, 739, 38
- Park, C., & Choi, Y.-Y. 2005, *ApJ*, 635, L29
- Roberts, M. S. 1963, *ARA&A*, 1, 149
- Portas, A. M., Brinks, E., Filho, M. E., et al. 2010, *MNRAS*, 407, 1674
- Saintonge, A., Kauffmann, G., Kramer, C., et al. 2011, *MNRAS*, 415, 32
- Saintonge, A., Kauffmann, G., Wang, J., et al. 2011, *MNRAS*, 415, 61
- Salim, S., Charlot, S., Rich, R. M., et al. 2005, *ApJ*, 619, L39
- Salim, S., Rich, R. M., Charlot, S., et al. 2007, *ApJS*, 173, 267
- Sandage, A. 1986, *A&A*, 161, 89
- Schiminovich, D., Wyder, T. K., Martin, D. C., et al. 2007, *ApJS*, 173, 315
- Schiminovich, D., Catinella, B., Kauffmann, G., et al. 2010, *MNRAS*, 408, 919
- Schlegel, D. J., Finkbeiner, D. P., & Davis, M. 1998, *ApJ*, 500, 525
- Schruba, A., Leroy, A. K., Walter, F., et al. 2011, *AJ*, 142, 37
- Serra, P., Oosterloo, T., Morganti, R., et al. 2012, *MNRAS*, 422, 1835
- Solanes, J. M., Sanchis, T., Salvador-Solé, E., Giovanelli, R., & Haynes, M. P. 2002, *AJ*, 124, 2440
- Springob, C. M., Haynes, M. P., & Giovanelli, R. 2005, *ApJ*, 621, 215
- Strauss, M. A., Weinberg, D. H., Lupton, R. H., et al. 2002, *AJ*, 124, 1810
- Toribio, M. C., Solanes, J. M., Giovanelli, R., Haynes, M. P., & Martin, A. M. 2011, *ApJ*, 732, 93
- Tremonti, C. A., Heckman, T. M., Kauffmann, G., et al. 2004, *ApJ*, 613, 898
- van Driel, W., van Woerden, H., Schwarz, U. J., & Gallagher, J. S., III 1988, *A&A*, 191, 201
- Walter, F., Brinks, E., de Blok, W. J. G., et al. 2008, *AJ*, 136, 2563
- Wang, J., Kauffmann, G., Overzier, R., et al. 2011, *MNRAS*, 412, 1081
- Wardle, M., & Knapp, G. R. 1986, *AJ*, 91, 23
- West, A. A., Garcia-Appadoo, D. A., Dalcanton, J. J., et al. 2009, *AJ*, 138, 796
- West, A. A., Garcia-Appadoo, D. A., Dalcanton, J. J., et al. 2010, *AJ*, 139, 315
- Wolfire, M. G., Hollenbach, D., & McKee, C. F. 2010, *ApJ*, 716, 1191
- Wong, O. I., Ryan-Weber, E. V., Garcia-Appadoo, D. A., et al. 2006, *MNRAS*, 371, 1855
- Wyder, T. K., Martin, D. C., Schiminovich, D., et al. 2007, *ApJS*, 173, 293
- Zhang, W., Li, C., Kauffmann, G., et al. 2009, *MNRAS*, 397, 1243

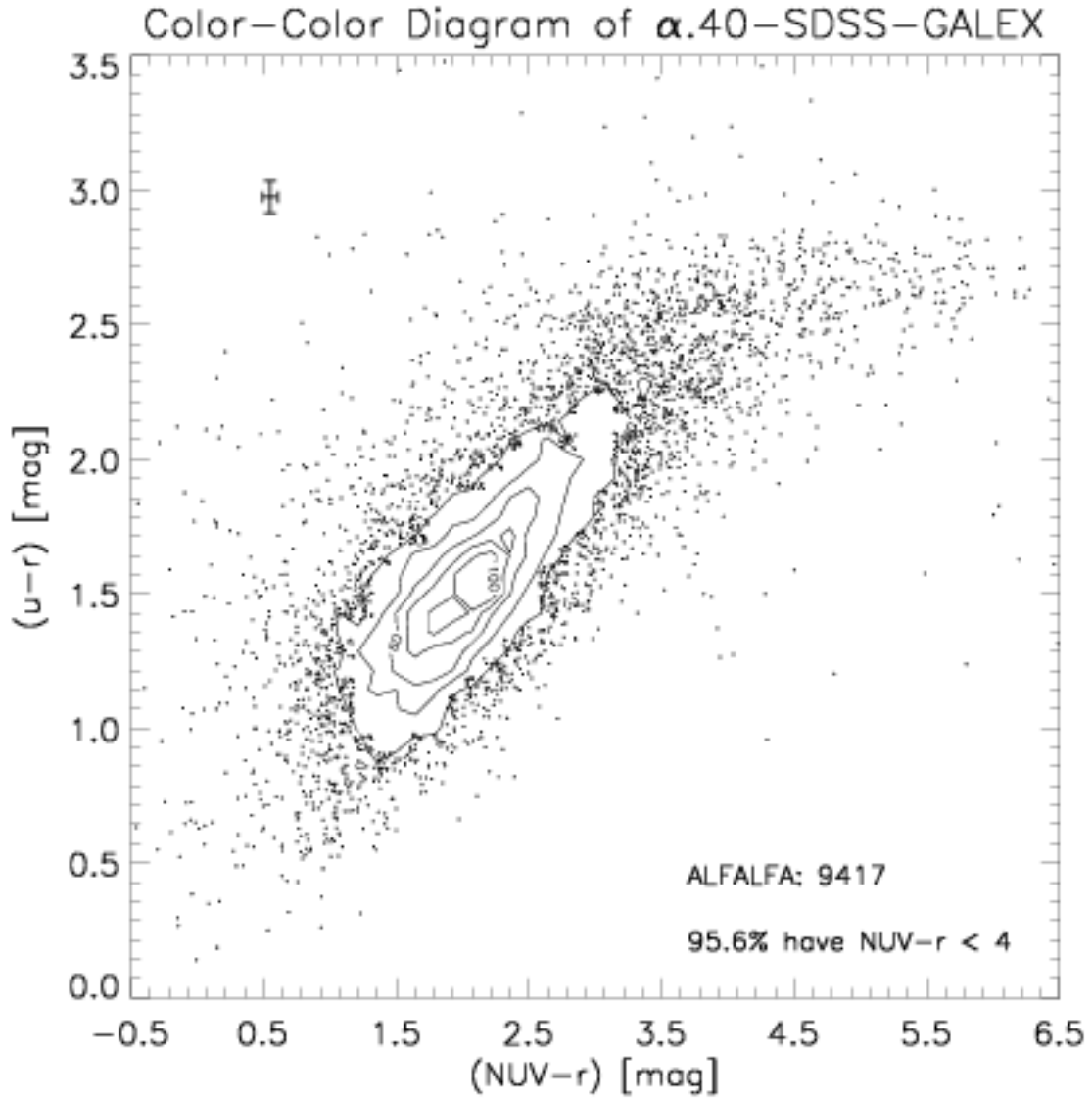


FIG. 1.— UV-optical color-color diagram. Contours and points represent the $\alpha.40$ -SDSS-GALEX common sample. The number density of galaxies in each grid cell is labeled on selected contours, e.g., the lowest contour level beyond which scatter points are plotted is 20 galaxies per grid cell. The grid size is shown by the interval of minor ticks on both axes. Among these 9417 galaxies, 96% have $(NUV-r) < 4$ and thus lie in the blue cloud by the criteria of Salim et al. (2007). The $(NUV-r)$ and $(u-r)$ colors are well correlated among the blue galaxies, with a slope of $\delta(u-r)/\delta(NUV-r) \sim 0.6$, but the distribution flattens among the reddest population. The $(NUV-r)$ color serves as a stronger diagnostic of SFH than colors derived only from the optical bands.

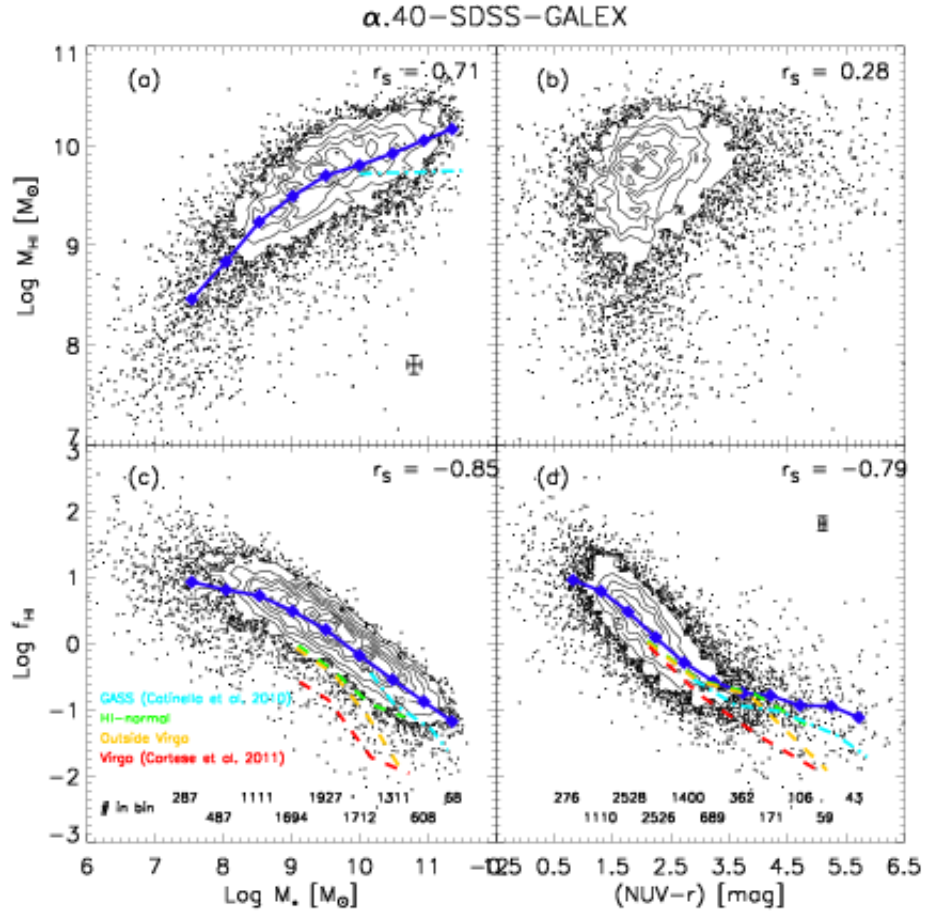


FIG. 2.— Scaling relations between HI mass, stellar mass and color. Contours and points follow the definitions in Figure 1. Blue diamonds and solid lines indicate the $\langle \log y \rangle$ values in each $\log x$ bin. The number of galaxies in each $\log x$ bin is listed at the bottom of panels (c, d). Cyan dash-dotted lines in panels (c, d) denote the average values of the GASS galaxies with $M_{*} > 10^{10} M_{\odot}$ (Catinella et al. 2010). Dashed lines in the same panels are from Cortese et al. (2011) derived for galaxies belong to different environments: 'HI-normal' (green on top), 'outside Virgo' (yellow in middle) and 'inside Virgo' (red at bottom). Typical error bars of individual galaxies are given in the corner of panels (a, d). Spearman's rank correlation coefficients, r_s , are listed in all panels.

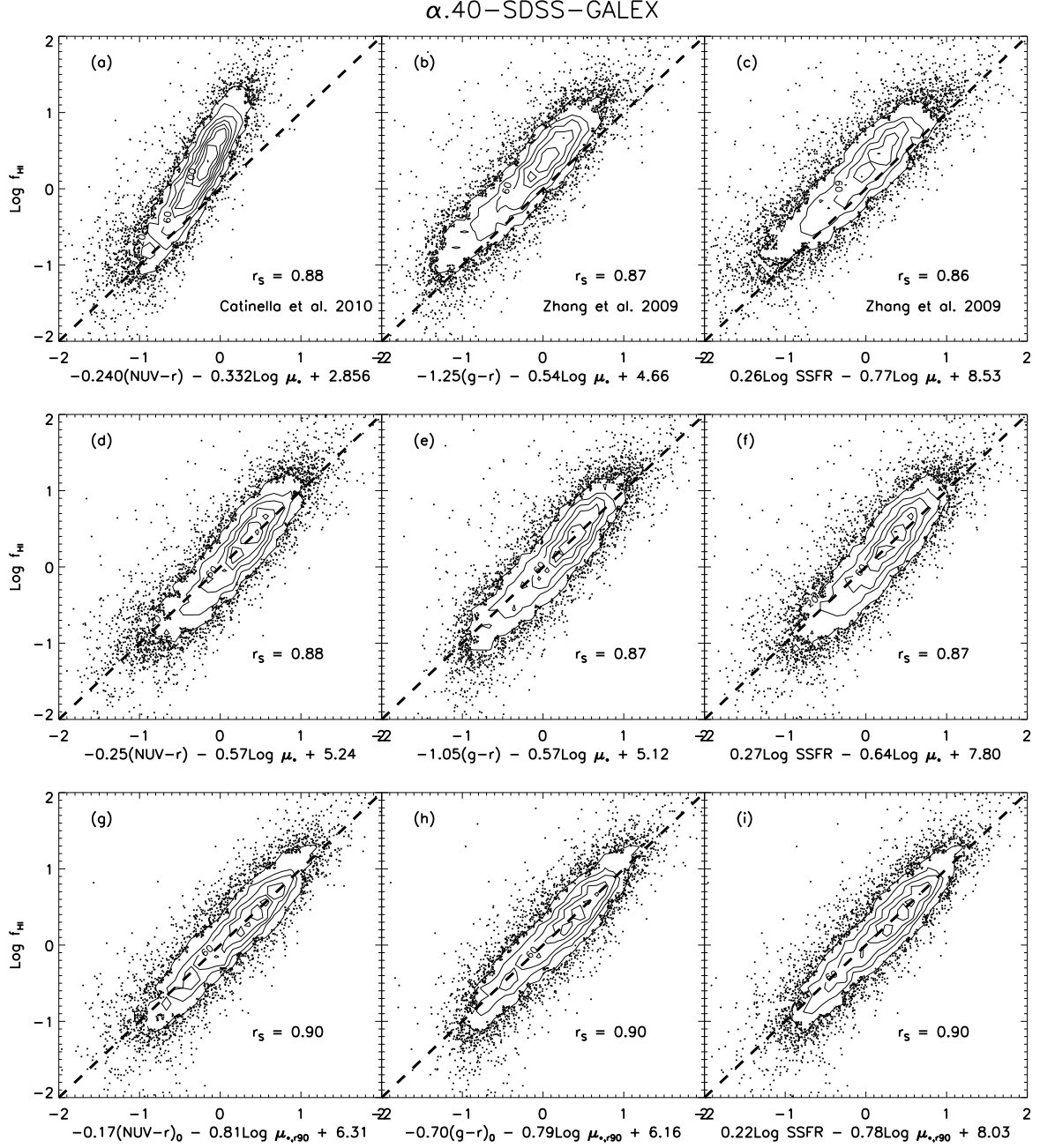


FIG. 3.— HI fraction estimators. Dashed lines are the one-to-one lines. Contours and points follow the definitions in Figure 1. Spearman’s rank correlation coefficients are shown in the lower right corners of all panels. *Upper panels* - The ALFALFA-observed f_{HI} versus the predicted values based on the fundamental planes calibrated from the GASS sample (Catinella et al. 2010) in panel (a), as well as from the SDSS-selected sample (Zhang et al. 2009) in panels (b) and (c). *Middle panels* - Observed f_{HI} versus the values predicted by the best fit to similar planes in this work, given the $\alpha.40\text{-SDSS-GALEX}$ sample. The systematic offsets are removed and the correlations are tighter. *Bottom panels* - Compared to the predictors in the middle row, the colors have been corrected for internal extinction and the stellar mass surface density is based on $r_{90,r}$, so that the scatter is reduced.

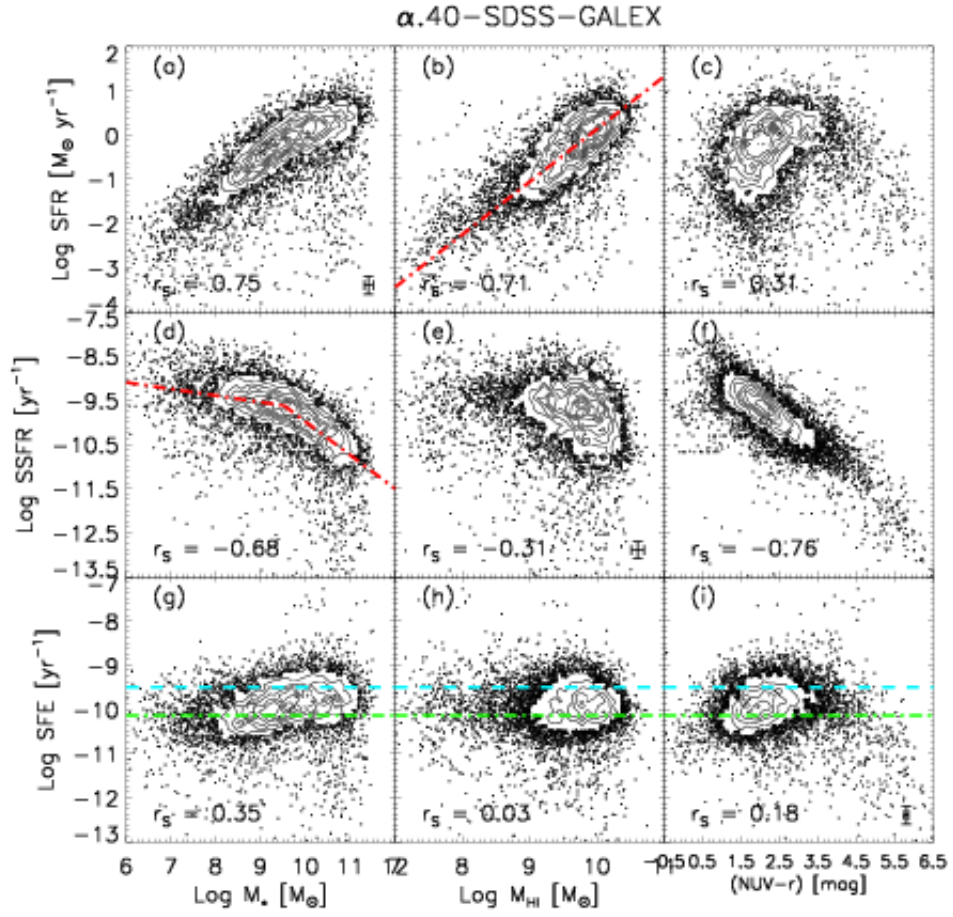


FIG. 4.— SF properties of the $\alpha.40$ -SDSS-GALEX population. Contours and points follow the definitions in Figure 1. Spearman's rank correlation coefficients are shown in the lower left corners of all panels. Colors here are not corrected for internal extinction. Typical error bars of individual galaxy estimates are plotted in the lower right corners of panels (a, e, i). The red dash-dotted line in panel (b), with a slope of 1.19, represents a global, atomic, volumetric SFL defined by the $\alpha.40$ -SDSS-GALEX galaxies. The red dash-dotted line in panel (d) represents the linear fit to the star-forming sequence given in equation (8). In the bottom row, tracing the SFE, the cyan dashed line shows the average value obtained by Schiminovich et al. (2010) for the GASS sample, while the green dash-dotted line corresponds to the Hubble timescale.

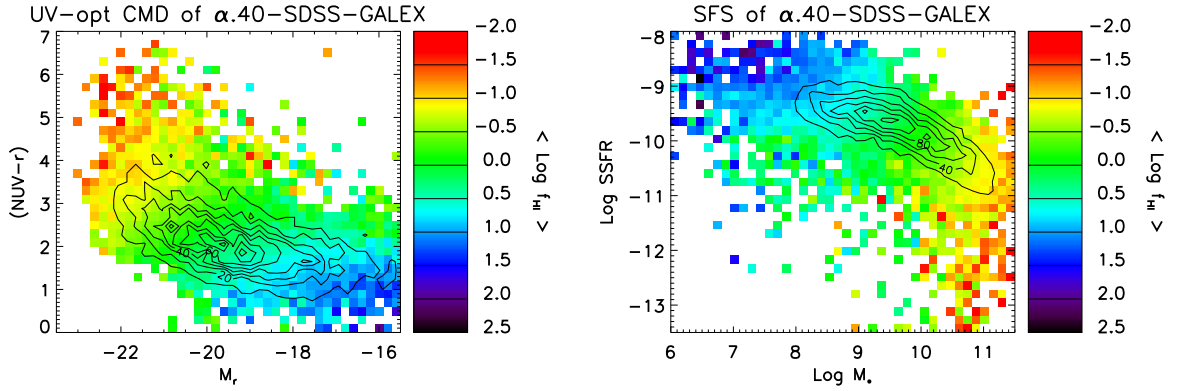


FIG. 5.— Diagrams of the $\alpha.40$ -SDSS-GALEX sample with shade scale showing the averaged HI fraction in each grid, while number density is indicated by the contours. *Left panel* - UV-to-optical CMD. The blue cloud galaxies dominate in number and are associated with higher f_{HI} on average. At given M_r , a redder $(NUV - r)$ color on average indicates lower f_{HI} ; this trend is more evident at the faint end. *Right panel* - The star forming sequence as traced by the contours. As galaxies assemble M_* and evolve along the sequence, their HI fractions follow a decreasing trend. At a fixed M_* , galaxies with lower SSFRs on average have lower f_{HI} , which is also more evident among low mass galaxies with $M_* \lesssim 10^{9.5} M_\odot$. The broadenings of the distributions of color, SSFR and f_{HI} at the low mass end are correlated to each other. (A color version of this figure is available in the online journal.)

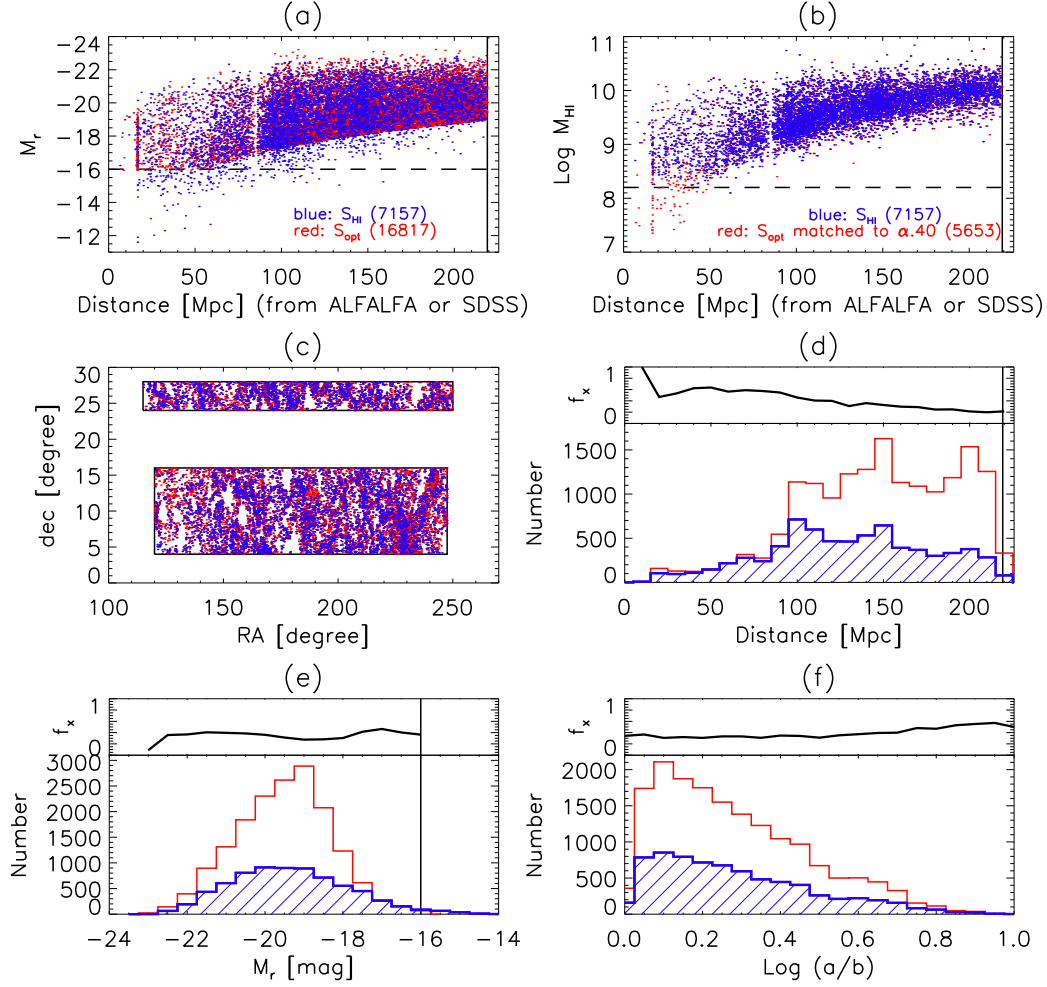


FIG. 6.— Comparison of the basic properties relevant to the sample selection of the HI-selected sample S_{HI} (7157 galaxies selected from the $\alpha.40$, blue points and blue histograms) and the optically-selected one S_{opt} (16817 galaxies selected from the SDSS, red points and red histograms). The panels above the histograms show the fraction of the S_{opt} galaxies that are cross-matched to $\alpha.40$ in each bin, similar to an HI detection rate of the S_{opt} galaxies by ALFALFA. Both samples are extracted from the same sky area (panel c), lie within $cz = 15000 \text{ km s}^{-1}$ (panel d) and are cross-matched to the GALEX catalog. Spaenhauer diagrams are in panels (a) and (b), i.e. r -band absolute magnitude, M_r , and M_{HI} against distance. A weight (or volume correction) cut of 60 applied on S_{opt} results in M_r brighter than ~ -16 , whereas applied on S_{HI} results in $M_{HI} \gtrsim 10^{8.2} M_{\odot}$. Though the two samples probe similar M_r ranges (panel e), the SDSS is deeper than ALFALFA, as evident in the distance distribution (panels d). No bias against edge-on galaxies in the S_{HI} population is seen in panel (f). (A color version of this figure is available in the online journal.)

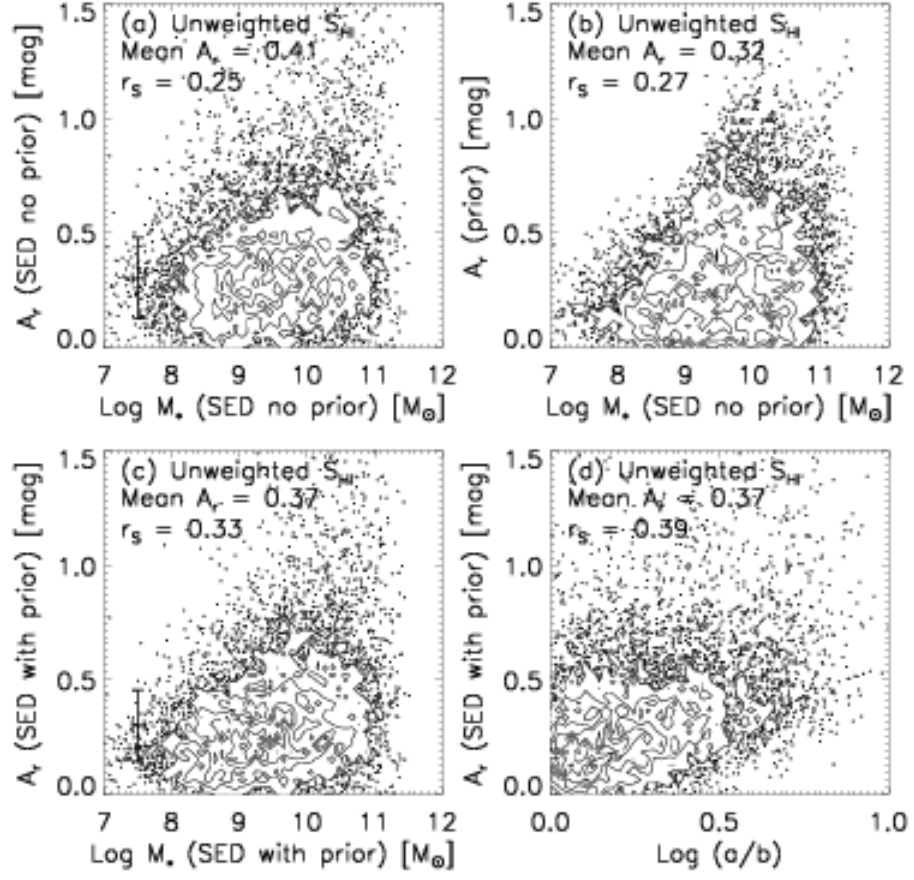


FIG. 7.— *Panels (a-c)* - The r -band internal extinction versus stellar mass. The values in panel (a) are derived by SED-fitting without the application of a prior τ_V distribution. The mean of the prior distribution is plotted in panel (b), based on equation (12) in Giovanelli et al. (1997). The SED-fitting has been improved by adopting the prior τ_V distribution as evident in panel (c). Internal extinction is a weakly increasing function of M_* with the greatest correlation, with a coefficient = 0.33, shown in panel (c). *Panel (d)* - Internal extinction is systematically higher in more inclined galaxies, as expected.

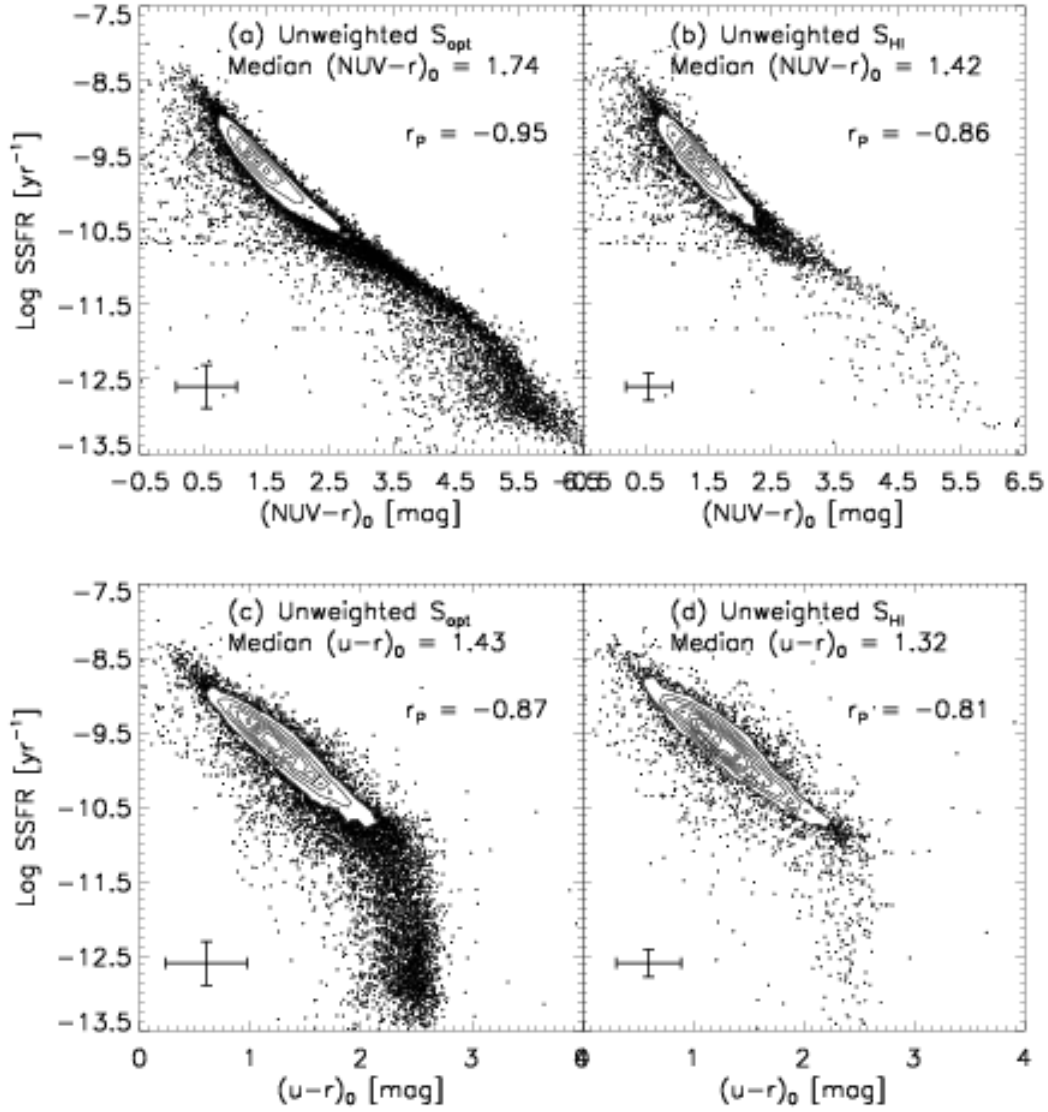


FIG. 8.— $SSFR$ versus intrinsic colors, denoted by the subscript zero, after correction for internal extinction. The left column shows results for S_{opt} while the right shows S_{HI} . Pearson correlation coefficients and typical error bars are also shown and the median intrinsic colors are indicated. In addition to the blueward shift of the distribution in panel (b) the scatter here is also greatly reduced compared to the similar plot shown in Figure 4(f) where no internal extinction correction has been applied. The $(NUV - r)$ color breaks the degeneracy of $(u - r)$ in the red range when inferring the SFH. The red and low SSFR tail in S_{opt} disappears in S_{HI} . S_{HI} is on average intrinsically bluer than S_{opt} in both colors.

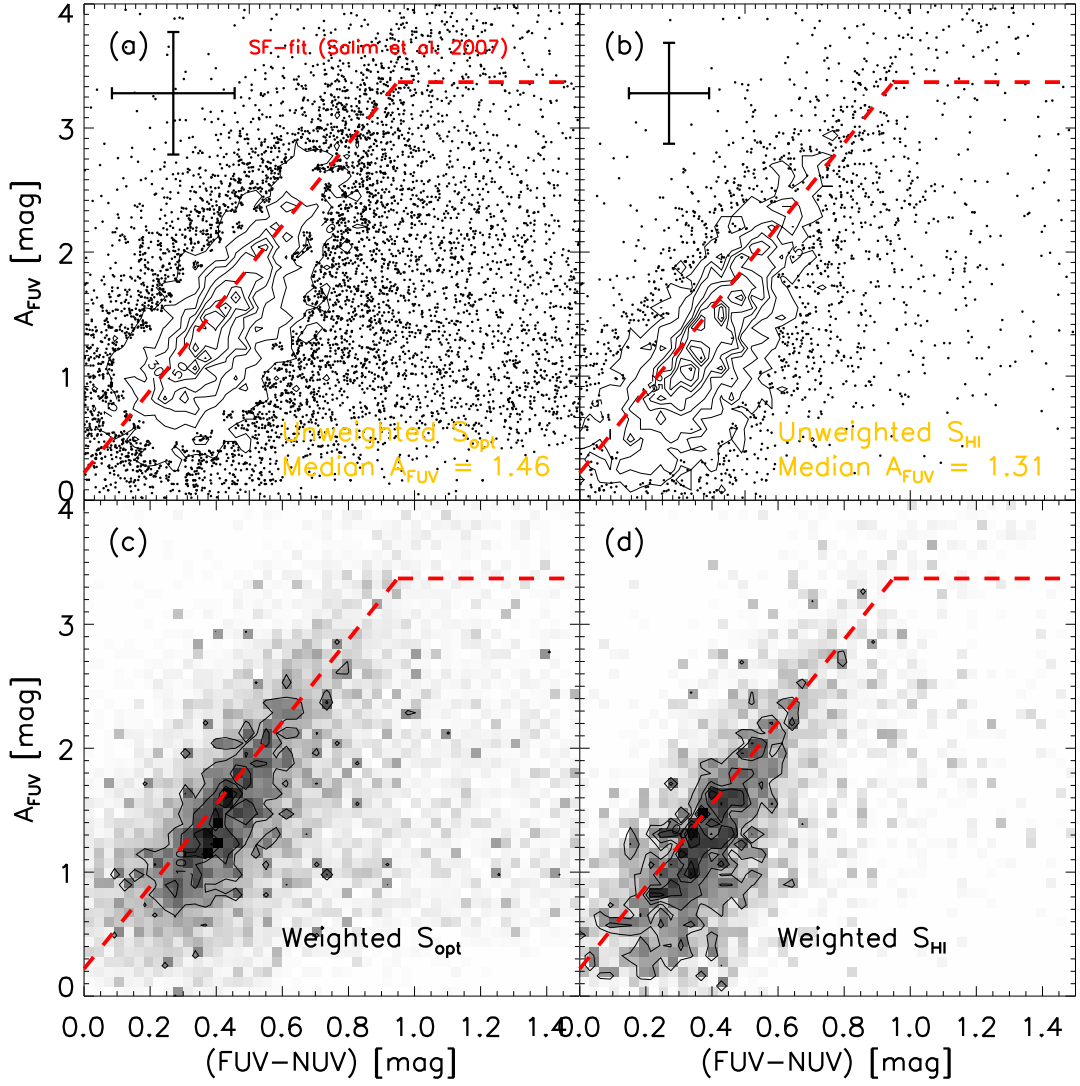


FIG. 9.— Computed $A_{FUV} - UV$ color diagrams for S_{opt} in the left column and S_{HI} in the right column. The upper row shows the results for the galaxies themselves, without weighting while the bottom row shows results after applying the V_{sur}/V_{max} weighting scheme. Typical error bars are shown in the corners of panels (a) and (b), together with the median A_{FUV} values listed for both the samples. The red dashed line corresponds to the fit to the star-forming galaxies derived by Salim et al. (2007), based on a typical local SDSS-GALEX cross-matched catalog. It is in agreement with S_{opt} . In contrast, the S_{HI} distribution is offset from the fit, with lower A_{FUV} at a fixed $(FUV - NUV)$ color, which may due to lower metallicity, different SFH, and/or dust geometry of the HI-selected galaxies.

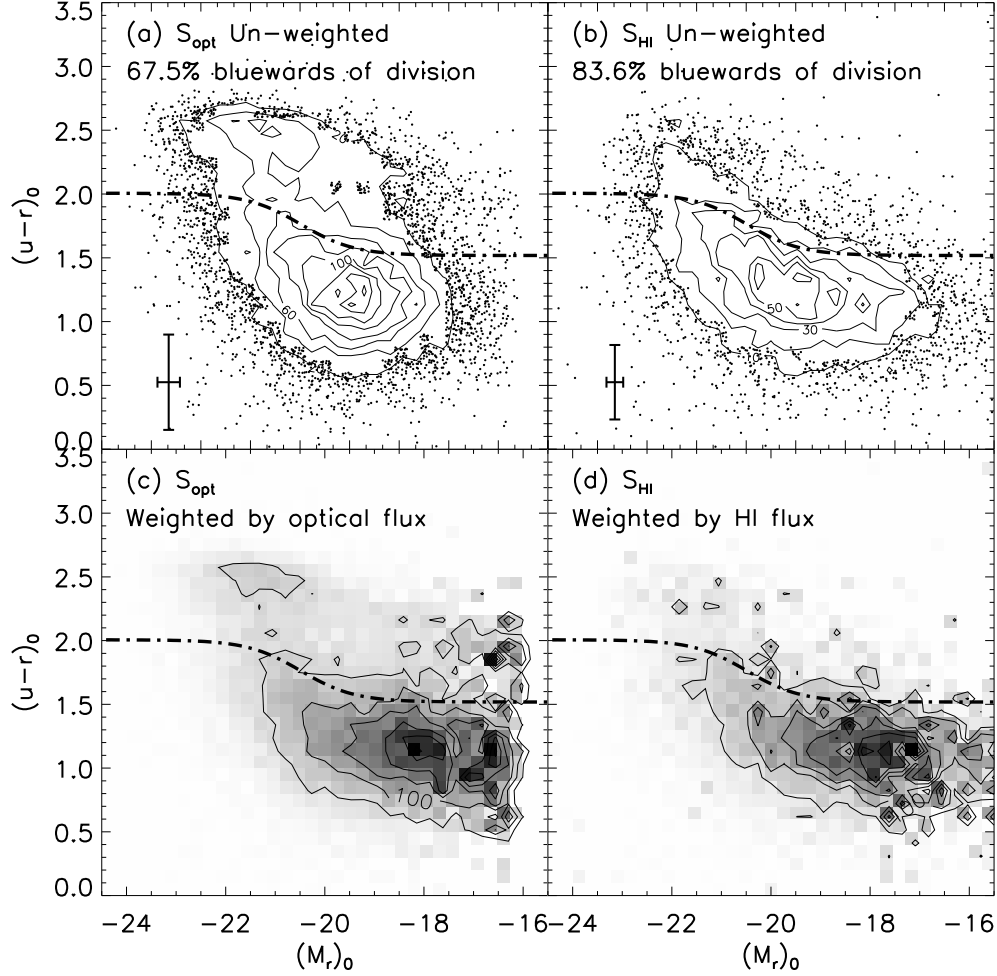


FIG. 10.— Intrinsic optical color-magnitude diagram of S_{opt} (left panels) and S_{HI} (right panels); before (upper) and after (lower) applying the V_{sur}/V_{max} weight correction. The dash-dotted curve is derived in Baldry et al. (2004) as the best fit to the division of red sequence and blue cloud, shifted for the extinction corrections. Typical error bars including the uncertainties in the extinction corrections are plotted in the lower left corner of panels (a) and (b). The bimodal distribution is more evident in the S_{opt} representations; colors become generally bluer in fainter galaxies for both populations. The weighted panels better represent the luminosity function, which predicts more faint galaxies relative to the bright ones in the blue cloud. However, a second peak of number density at the faint end is seen on the red sequence, which suggests a diversity of SFH within the dwarf galaxies. A higher percentage of galaxies lie bluewards of the division in S_{HI} (84%) relative to S_{opt} (67.5%). HI surveys such as ALFALFA are highly biased against red sequence galaxies.

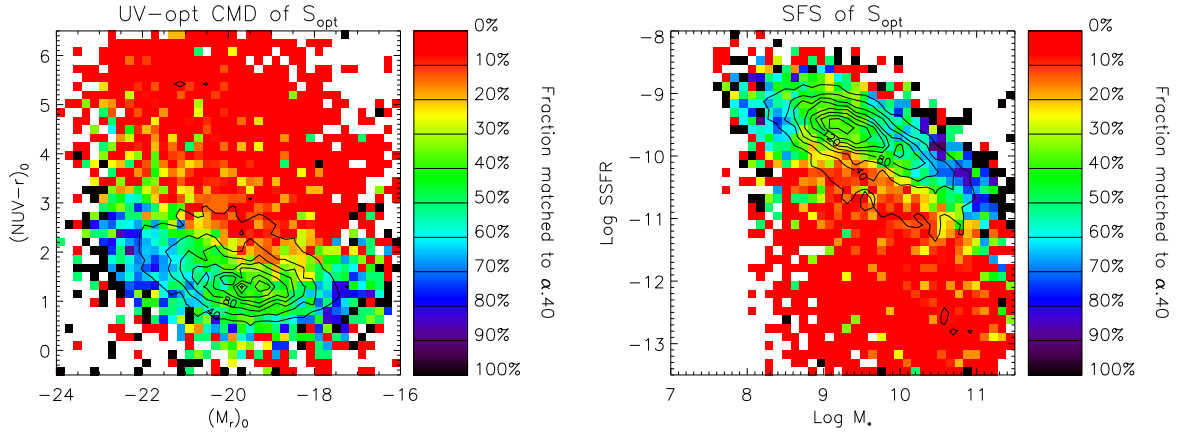


FIG. 11.— Diagrams with shade scale showing the fraction of galaxies in S_{opt} that are cross-matched to the $\alpha.40$ in each grid, which is close to the HI detection rate of the S_{opt} by $\alpha.40$. The S_{opt} number density is indicated by the contours. The cross-match fraction is the lower limit of the detection rate of S_{opt} galaxies by $\alpha.40$; its overall average is 34%. *Left panel* - Intrinsic UV-to-optical CMD of S_{opt} . ALFALFA is more efficient in detecting blue galaxies, especially (i) the very bright and blue galaxies with huge gas reservoirs and (ii) the galaxies with the highest HI fraction lie on the faint end of the blue cloud. However, starting from the redder edge of the blue cloud, the cross-match rate drops below 10% and to even $\sim 0\%$ throughout most of the red sequence. *Right panel* - SSFR versus stellar mass for the S_{opt} galaxies. The cross-match rate is the highest among the galaxies with high SSFRs at both high and low stellar mass ends and is close to the overall average throughout the high number density region along the star forming sequence. However, it drops to below $\sim 20\%$ from the lower edge of the sequence to even $\sim 0\%$ in the low SSFR regime.
(A color version of this figure is available in the online journal.)

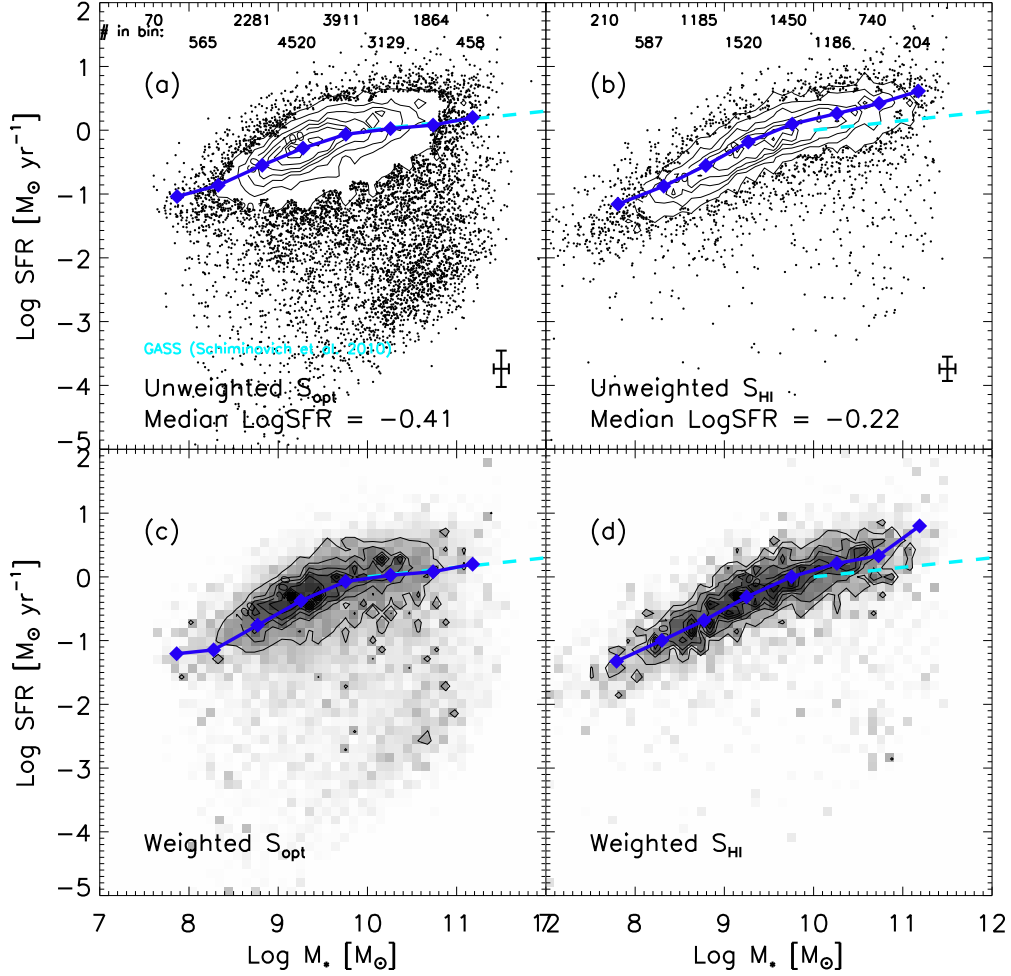


FIG. 12.— SFR versus M_* for the S_{opt} (left) and the S_{HI} (right) samples; upper panels show the individual galaxies while the low ones show the results of applying the V_{sur}/V_{max} weighting. The cyan dashed lines above $M_* = 10^{10} M_\odot$ show the fit to this relation obtained by Schiminovich et al. (2010), based on the GASS sample. The blue diamonds and lines represent the corresponding $\log\langle SFR \rangle$ of our datasets. The number of galaxies in each stellar mass bin is listed at the top in panels (a) and (b), together with the typical error bars plotted in the lower right corners. The median SFRs for both the samples are indicated. The GASS fit is consistent with the distribution seen for the S_{opt} sample but is systematically below the average of the HI-selected galaxies. The slope of the relation appears to steepen below $M_* \sim 10^{9.5} M_\odot$. The S_{HI} sample has a higher overall SFR value than the S_{opt} galaxies, and probes to slightly lower M_* ranges with generally lower SFRs. The data points reveal a concentration of massive low SFR galaxies below the main trend in S_{opt} , which are largely absent from the S_{HI} population. An HI survey samples the star-forming population. The flattening of the trend in the lowest mass bin in the S_{opt} plots is artificial, due to the weight cut applied.

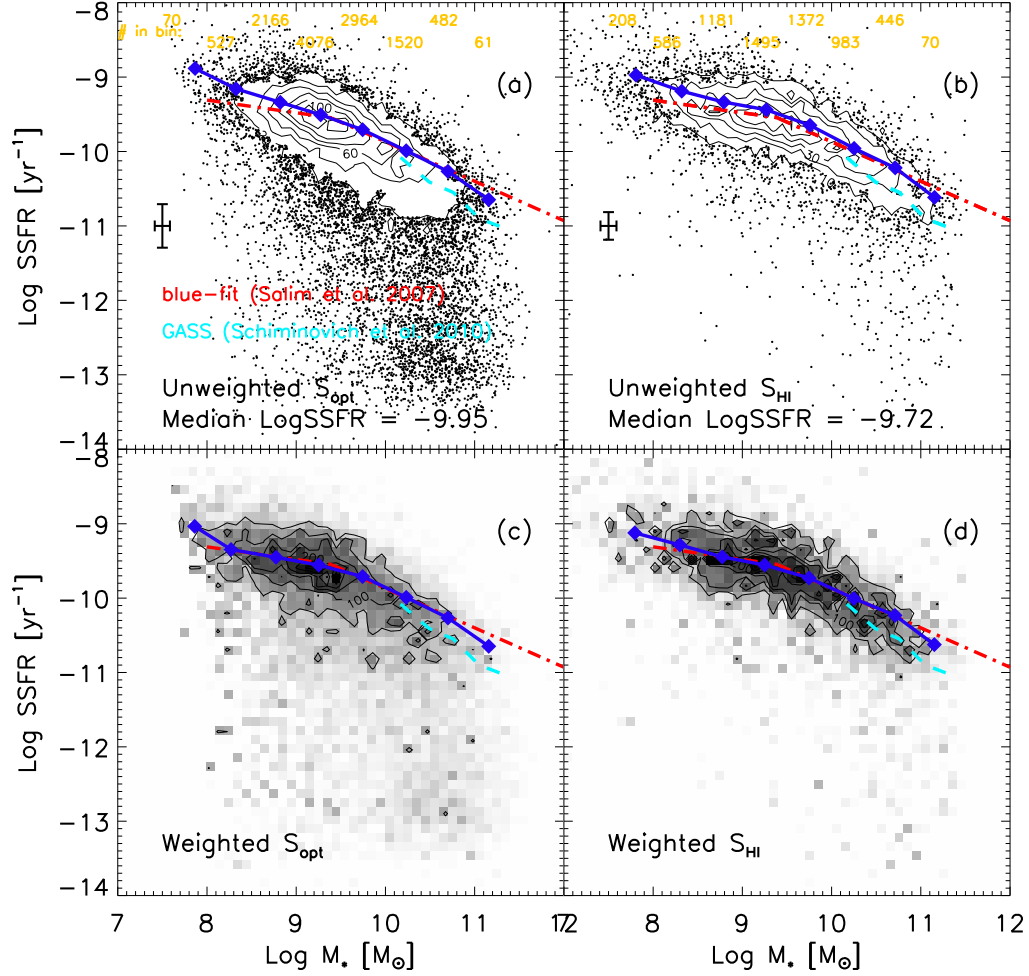


FIG. 13.— Similar diagrams of $SSFR$ versus M_* . The numbers of galaxies in each stellar mass bin are listed, as well as the median SSFRs for both samples. The contours outlying the high number density region roughly trace the star forming sequence. The red dashed line shows the fit to such a sequence of the blue galaxies with $(NUV - r) < 4$ (Salim et al. 2007), derived from a typical local SDSS-GALEX cross-matched catalog, with the majority confined to the stellar mass range $10^8 - 10^{10} M_\odot$. The blue diamonds and lines are obtained by applying the same color criteria to the S_{opt} or S_{HI} galaxies. The cyan dashed line comes from Schiminovich et al. (2010) based on the high M_* GASS sample; it well represents the contours of S_{opt} , but lies systematically below the average of S_{HI} . When only blue galaxies are considered in both samples, the discrepancy between the main trend of S_{opt} and S_{HI} is small. Furthermore, both agree well with the red dashed line. Galaxies selected by HI criteria have on average higher SSFRs than optically-selected ones. The breakdown of the star forming sequence above $M_* \sim 2 \times 10^{10} M_\odot$ is only evident among the S_{opt} sample, whereas the S_{HI} galaxies are strongly biased against massive and low SSFR galaxies.

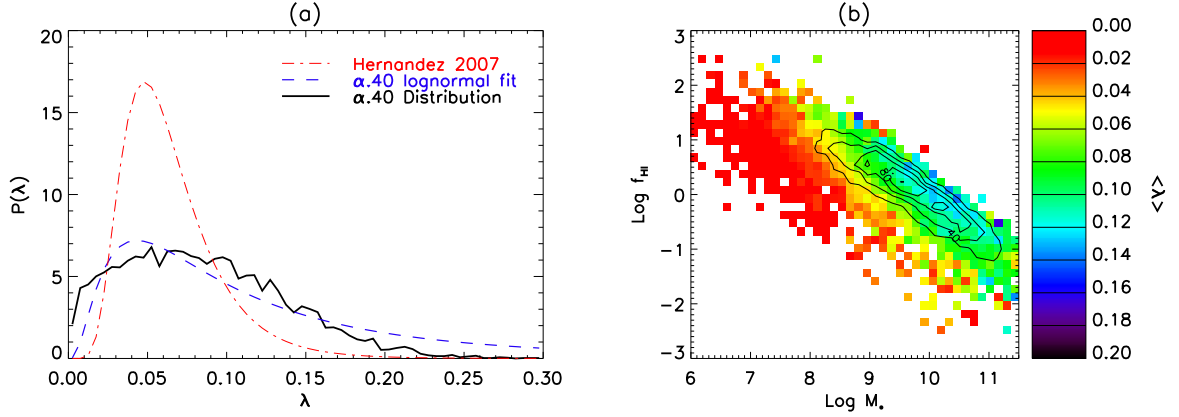


FIG. 14.— Spin parameter λ distribution obtained by assigning the M_{halo} through a $V_{rot}-V_{halo}$ relationship. *Panel (a)* - The black solid line is the normalized PDF of the λ distribution of 7459 galaxies from the $\alpha.40$ -SDSS-GALEX sample. The blue dashed line is the best lognormal fit to the distribution. The red dash-dotted line is the lognormal fit to a sample of spiral galaxies from the SDSS, assuming constant baryonic mass fraction $F = 0.04$ ($\lambda_0 = 0.0585$ Hernandez et al. 2007). The λ distribution of the $\alpha.40$ galaxies has a higher mean λ (0.0852) and a wider dispersion, mainly arising from the adopted distribution of baryonic fraction. *Panel (b)* - f_{HI} vs. M_* diagram color coded by the mean λ values of the galaxies in each grid. Below $M_* \sim 10^{10.5} M_{\odot}$, $\langle \lambda \rangle$ increases with increasing f_{HI} at a given M_* , but remains almost constant along constant M_{HI} lines. Such a trend reflects the adopted variation of F : HI-selected gas-rich galaxies favor high λ halos.
(A color version of this figure is available in the online journal.)